MOX–Report No. 08/2014

A computational model of drug delivery through microcirculation to compare different tumor treatments

Cattaneo, L; Zunino, P.

MOX, Dipartimento di Matematica "F. Brioschi"
Politecnico di Milano, Via Bonardi 9 - 20133 Milano (Italy)

mox@mate.polimi.it http://mox.polimi.it

A computational model of drug delivery through microcirculation to compare different tumor treatments

Laura Cattaneo[♯] and Paolo Zunino[♯,†]

February 3, 2014

[♯] MOX– Modellistica e Calcolo Scientifico
Dipartimento di Matematica "F. Brioschi"
Politecnico di Milano
via Bonardi 9, 20133 Milano, Italy
laura1.cattaneo@polimi.it

[†] Department of Mechanical Engineering and Materials Science
University of Pittsburgh
3700 O'Hara Street, Pittsburgh, PA 15261, USA
paz13@pitt.edu

Keywords: blood perfusion; mass transport; microvascular environment; drug delivery;

Abstract

Starting from the fundamental laws of filtration and transport in biological tissues, we develop a computational model to capture the interplay between blood perfusion, fluid exchange with the interstitial volume, mass transport in the capillary bed, through the capillary walls and into the surrounding tissue. These phenomena are accounted at the microscale level, where capillaries and interstitial volume are viewed as two separate regions. The capillaries are described as a network of vessels carrying blood flow. We apply the model to study drug delivery to tumors. The model can be adapted to compare various treatment options. In particular, we consider delivery using drug bolus injection and nanoparticle injection into the blood stream. The computational approach is prone to a systematic quantification of the treatment performance, enabling the analysis of interstitial drug concentration levels, metabolization rates and cell surviving fractions. Our study suggests that for the treatment based on bolus injection, the drug dose is not optimally delivered to the tumor interstitial volume. Using nanoparticles as intermediate drug carriers overrides the shortcomings of

the previous delivery approach. The present work shows that the proposed theoretical and computational framework represents a promising tool to compare the efficacy of different cancer treatments.

1 Introduction and motivations

Mass transport plays a fundamental role in the development of cancer. At different phases of cancer disease, such as the propagation of growth signals, the invasion of other tissue and the activation of angiogenesis, tumors use mass transport phenomena to interact with the surrounding environment [20]. Mass transport is also at the basis of cancer pharmacological treatment. Targeting vascularized tumors using the vascular network is a natural therapeutic option. Nevertheless, the success of anticancer therapies in treating cancer cells is limited by their inability to reach their target *in vivo* in adequate quantities [21]. An agent that is delivered intravenously reaches cancer cells via distribution through the vasculature, transport across the wall of the vessels and transport through the tissue interstitium. Each of these steps can be seen as a barrier to delivery. In addition, delivered molecules may bind to constituents of the extracellular matrix and be metabolised by cells.

The characteristic traits of cancer can be seen as the emergent effects of a cascade of phenomena that propagate from the molecular scale, through the cell and the tissue microenvironment, up to the systemic level. Transport phenomena at the level of the capillary network (the microenvironment or microscale) play a key role in this sequence of effects. In particular, the alterations of the capillary phenotype of a tumor significantly affect the drug delivery process [7]. More precisely, blood vessels in tumors are leakier and more tortuous than the normal vasculature and the pressure generated by the proliferating cells reduces tumor blood and lymphatic flow. These perturbations lead to an impaired blood supply and abnormal tumor microenvironment characterized by hypoxia and elevated interstitial fluid pressure. They also reduce the ability to deliver drugs.

The objective of this work is to perform a comparative study of different modalities to deliver drug to a vascularized tumor mass. This is achieved by developing a new computational pharmacokinetic model able to capture the absorption of a drug through the vascular network as well as its distribution and metabolization in the tumor. Following the seminal sequence of works by Baxter and Jain [2, 3, 4, 5], we believe that the interplay between blood perfusion, fluid exchange with the interstitial volume, mass transport in the capillary bed, through the capillary walls and into the surrounding tissue, are important effects to understand the delivery process at the microscale. Temporal and spatial dependence will be fully accounted in our governing equations, in contrast to the approach based on compartment models. Since we consider these phenomena at the level of capillaries, it is possible to derive the governing equations from a mechanistic standpoint based on the fundamental laws of flow and mass

transport. The model is also prone to be adapted to different delivery methods. Besides studying the case of bolus injection, which consists in delivering a solution containing the active drug into the peripheral systemic circulation, we analyze the delivery of drug from nanoparticles, which are in turn injected into the blood stream and interact with the capillary walls.

The analysis of tissue perfusion and mass transport has been addressed using various advanced approximation approaches. Without any ambition to provide an exhaustive literature review, we mention [9, 25] where the problem of cardiac perfusion is addressed, [10, 34] where homogenization techniques are applied to characterize the average transport properties of tumor tissue constructs and [38] where isogeometric analysis is used to model angiogenesis in vascularized tumors.

The model that we develop ends up to be a system of partial differential equations, which are hard to solve with analytical tools. For this reason, we complement the model with a state of art numerical solver, based on the finite element method. The numerical scheme is based on the idea to represent the capillary bed as a network of one-dimensional channels that acts as a concentrated source of flow immersed into the interstitial volume, because of the natural leakage of capillaries. As a result, it can be classified as an *embedded multiscale* method. In the case of simple geometrical configurations of capillary vessels, such as an array of straight channels, semi-analytic solutions of the problem have been developed [6, 16, 15]. A more extensive application of numerical approximation methods has recently enabled the analysis of realistic microvascular geometries [21, 8, 33, 36]. Here, we extend this approximation strategy to problems involving blood flow and mass transport. The main advantage of the proposed scheme is that the computational grids required to approximate the equations on the capillary network and on the interstitial volume are completely independent. As a result, arbitrarily complex microvascular geometries may be potentially considered. From the standpoint of numerical approximation, the theoretical aspects of the method have been addressed in the works by D'Angelo [12, 13, 14].

Our results suggest that using nanoparticles as intermediate vectors for chemotherapy improves the treatment. For the same amount of injected dosage, drug charged nanoparticles provide higher concentration levels in the interstitial tissue of the tumor and more persistent delivery over time with respect to bolus injection. Thanks to the computational approach, these conclusions are based on the analysis of specific performance indicators, such as the interstitial drug concentration level, the drug metabolization rate, the cell surviving fraction and the corresponding timecourse.

2 Materials and methods

We start the derivation of the model by presenting the governing equations for microcirculation, tissue perfusion and mass transport. In a second phase, we will adapt these general equations to specific cases. The first case is the study of the coupled transport of oxygen and tirapazamine, a drug specifically designed to target hypoxic cells. In the second one we apply the theory to analyze the delivery of drugs consequent to the injection of nanoparticles into the tumor region.

We aim to model fluid and mass transport in a permeable biological tissue perfused by a capillary network. We consider a domain Ω that is composed by two parts, Ω_v and Ω_t, the capillary bed and the tumor interstitium, respectively. To account for the microvascular network, we model the capillaries as cylindrical vessels. We denote with Γ the outer surface of Ω_v, with R its radius and with Λ the centerline of the capillary network. A characteristic feature of the computational model is that the capillaries are actually represented as one-dimensional channels. As shown in [6, 15, 16, 33] this approximation significantly simplifies the problem at the computational level. This is done by taking the limit $R \to 0$ and shrinking the capillary bed to its centerline Λ. We denote with s the arc length coordinate along this line. A sketch of the domains before and after adopting the one-dimensional representation of the capillary network is visualized in Figure 1.

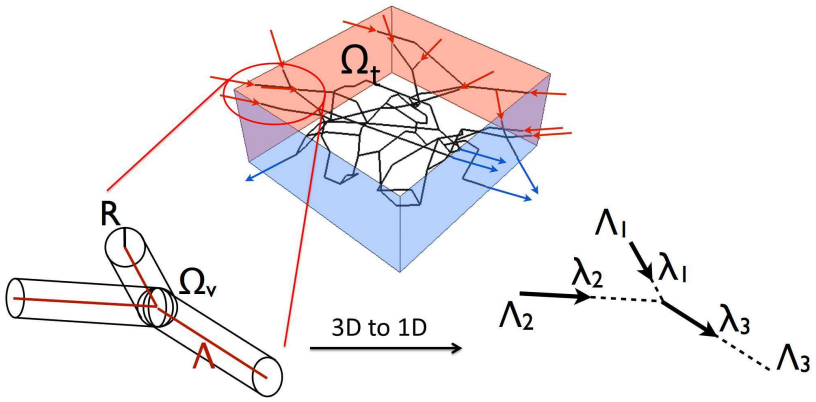

Figure 1: Visualization of a realistic vascular network that is used in the simulations, courtesy of Dr. T. Secomb, available online at [31]. The transition from a three-dimensional to a one-dimensional description of the vessels is depicted below. The colors on the sides of the tissue sample identify the inflow (red) and the outflow (blue) sections of the capillary network.

After this step, we observe that the distinction between the subregion Ω_t and the entire domain Ω is no longer meaningful, because Λ has null measure in $\mathbb{R}^d$. For notational convenience, in what follows we will then identify Ω_t with Ω and

Ω_v with Λ.

The physical quantities of interest are the flow pressure p, the velocity $\mathbf{u}$ and the concentration of transported solutes c. They are all defined as fields depending on time t and space, being $\mathbf{x} \in \Omega$ the spatial coordinates. Furthermore, we denote with the subscript v their restriction to the capillary bed (vessels), and with t the restriction to the interstitial tissue. The derivation of our model stems from fundamental balance laws regulating the flow in the capillary bed, the extravasation of plasma and solutes and their transport in the interstitial tissue.

2.1 Governing equations for flow and mass transport

The flow model consists in two parts, the microcirculation and the flow in the interstitial volume, which interact through suitable interface conditions. We assume that the tumor interstitium behaves as an isotropic porous medium. The flow through the interstitium is modelled by the Darcy's law. A Newtonian model is applied for the blood flow in the capillaries. We want to take into account of the lymphatic drainage, which plays an important role in the phenomena we aim at studying [8, 35].

Microcirculation is an extreme case where the size of vessels is the smallest and the effect of blood pulsation is almost negligible. The Reynolds and the Womersley numbers characterizing the flow are very low if compared to other regions of the vascular network. As a result, Poiseuille's law for laminar stationary flow of incompressible viscous fluid appropriately describes this flow [2, 6]. Let us decompose the network Λ into individual branches Λ_i, $i = 1, \ldots, N$. We denote with $\boldsymbol{\lambda}_i$ an arbitrary orientation of each branch that defines the increasing direction of the arc length s_i (see also Figure 1). Let $\boldsymbol{\lambda}$, s be the same quantities referring to the entire newtwork Λ.

One of the functions of the capillary network is to transport and distribute fluid and chemicals to the interstitial volume. This is achieved by means of the leakage of the capillary walls. We model this effect using the Kedem-Katchalsky equation, that is

$$J_v := L_p((p_v - p_t) - \sum_k \sigma_k(\pi_{v,k} - \pi_{t,k}))$$

where L_p is the hydraulic conductivity of the vessel wall (see Table 1 for units and physiological values). Because of osmosis, the pressure drop across the capillary wall is affected by the difference in concentration of the chemicals dissolved in blood, [11, 18], denoted here with the index k. This gives rise to the oncotic pressure transmural gradient, namely $\pi_{v,k} - \pi_{t,k}$, where $\pi = R_g T c$ is the oncotic pressure given by a concentration c of a given solute, being R_g the universal gas constant and T the absolute temperature. The oncotic pressure is modulated by the reflection coefficient σ_k that quantifies the departure of a semi-permeable membrane from the ideal permeability (where any molecule is

able to travel across the membrane without resistance). Although the index k spans over all solutes that are dissolved in blood, not all of them significantly affect the oncotic pressure. Only the large molecules, such as proteins, can induce a significant oncotic pressure gradient. Indeed, the oncotic pressure gradient is mainly due to the significant presence of albumin in blood, whose concentration can be reasonably considered to be constant. According to data provided in [11, 18, 28], the oncotic pressure gradient due primarily to albumin in arterioles and capillaries is about 25 mmHg, which is comparable to the hydrostatic pressure in the vessel. In contrast, we assume that solutes such as oxygen or low concentrated drugs can not significantly contribute. This assumption will be further discussed in what follows, on the basis of the physical parameters characterizing the transport of the considered solutes (see Tables 1, 2). As a result, for our purposes, the capillary leakage only depends on the hydrostatic pressure according to the following expression,

$$J_b(p_t, p_v) := L_p((p_v - p_t) - \sigma(\pi_v - \pi_t)) = L_p((p_v - p_t) - \sigma_p R_g T(c_{v,p} - c_{t,p})) \quad (1)$$

where, in agreement with the definition of π, $c_{v,p}$ and $c_{t,p}$ denote the constant protein concentration in the capillaries and the interstitial tissue respectively. As a consequence, the flow equations do not depend on the mass transport model that will be developed in the next section.

To contrast capillary leakage, the venous and the lymphatic systems absorb the fluid in excess. Following [3] and [35], we model them as a distributed sink term in the equation for the tissue perfusion. More precisely, we assume that the volumetric flow rate due to lymphatic vessels, Φ^{LF}, is proportional to the pressure difference between the interstitium and the lymphatics, namely $\Phi^{LF}(p_t) = L_p^{LF}\frac{S}{V}(p_t - p_L)$, where L_p^{LF} is the hydraulic conductivity of the lymphatic wall, S/V is the surface area of lymphatic vessels per unit volume of tissue and p_L is the hydrostatic pressure within the lymphatic channels. The values of these parameters with the corresponding units are listed in Table 1. The coupled problem for microcirculation and perfusion consists to find the pressure fields p_t, p_v and the velocity fields $\mathbf{u}_t$, $\mathbf{u}_v$ such that

$$\begin{cases} -\nabla \cdot \left(\dfrac{k}{\mu}\nabla p_t\right) + L_p^{LF}\dfrac{S}{V}(p_t - p_L) - f_b(\overline{p}_t, p_v)\delta_\Lambda = 0 & \text{in } \Omega \quad (2a) \\ \mathbf{u}_t = -\dfrac{k}{\mu}\nabla p_t & \text{in } \Omega \quad (2b) \\ -\dfrac{\pi R^4}{8\mu}\dfrac{\partial^2 p_v}{\partial s^2} + f_b(\overline{p}_t, p_v) = 0 & s \in \Lambda \quad (2c) \\ \mathbf{u}_v = -\dfrac{R^2}{8\mu}\dfrac{\partial p_v}{\partial s}\boldsymbol{\lambda} & s \in \Lambda \quad (2d) \end{cases}$$

$$f_b(\overline{p}_t, p_v) := 2\pi R L_p((p_v - \overline{p}_t) - \sigma(\pi_v - \overline{\pi}_t))$$

where the term $f_b(\overline{p}_t, p_v)\delta_\Lambda$ accounts for the blood flow leakage from vessels to tissue and it has to be understood as the Dirac measure concentrated on Λ, denoted with δ_Λ, and having line density f_b. For an appropriate dimensional interpretation of equation (2a), we remind that δ_Λ is not a dimensionless function. According to its definition $\int_\Omega f\delta_\Lambda (dx)^3 = \int_\Lambda f ds$, the dimension of δ_Λ is $[\text{length}]^{-2}$. Equation (2c) represents Poiseuille flow on the capillary network. Since the capillary bed is modelled as a one-dimensional network embedded into the interstitial volume, the equations would be ill posed if the coupling between the two subregions was considered pointwise [13, 14]. For this reason, the function $f_b(\overline{p}_t, p_v)$ is such that the capillary bed is affected by the average of quantities in the interstitial tissue, calculated on a cylindrical surface that represents the actual size of capillaries (see Figure 1 for a sketch). The average value of pressure, velocity or concentration fields over the real surface of the capillary bed is denoted by

$$\overline{g}(s) := \frac{1}{2\pi R}\int_0^{2\pi} g(s,\theta) R d\theta.$$

For a more detailed derivation of this model from the problem formulation where also the capillaries are modelled as three-dimensional channels, we refer the interested reader to [8].

To model drug transport in the interstitial tissue we assume that molecules are advected by the fluid and diffuse in all Ω. In addition chemical species may be metabolised by the cells in the interstitial tissue. The distribution of solutes in the interstitial tissue is also affected by the lymphatic drainage. According to the assumptions at the basis of the flow model, the effect of lymphatic drainage on mass transport is described as a distributed sink proportional to $L_p^{LF}\frac{S}{V}(p_t - p_L)c_t$.

Mass transport in the capillary bed is modelled by means of advection-diffusion equations. As shown in [12], the one dimensional model for mass transport in the capillaries network can be derived starting from the actual 3D advection-diffusion problem. The coupled problem, accounting for transport of chemicals from the microvasculature to the interstitium, consists to find the concentrations c_v and c_t respectively, such that

$$\begin{cases} \dfrac{\partial c_v}{\partial t} + \dfrac{\partial}{\partial s}(|\mathbf{u}_v| c_v - D_v \dfrac{\partial}{\partial s} c_v) = -\dfrac{1}{\pi R^2} f_c(\overline{p}_t, p_v, \overline{c}_t, c_v) & \text{in } \Lambda \qquad (3a) \\ \dfrac{\partial c_t}{\partial t} + \nabla\cdot(c_t \mathbf{u}_t - D_t \nabla c_t) + m c_t + L_p^{LF}\dfrac{S}{V}(p_t - p_L)c_t = \\ \qquad = f_c(\overline{p}_t, p_v, \overline{c}_t, c_v)\delta_\Lambda & \text{in } \Omega \qquad (3b) \end{cases}$$

where D_v and D_t are the molecular diffusivities, in the capillaries and the interstitium, respectively, assumed to be constant in each region. The rate of metabolization in the interstitium is denoted by m. This parameter may in turn be a function of the concentrations, as it will be pointed out later on (see Table 2

for values and units). The function $f_c(\overline{p}_t, p_v, \overline{c}_t, c_v)$ is a mass flux per unit length of the capillary vessels and it accounts for the mass transfer from the capillary bed to the interstitial tissue. The concentration in the vascular network, c_v, is defined as mass per unit volume, therefore the linear concentration is given by Ac_v, being $A = \pi R^2$ the cross sectional area of a blood vessel. In order to restore the dimensional homogeneity of equations (3a) and (3b), we divide all the terms of (3a) by πR^2. As a result, the factor $(\pi R^2)^{-1}$ multiplies the last term of (3a). We describe the capillary walls as *semipermeable membranes* allowing not only for the leakage of fluid, but also for the selective filtration of molecules. Again, the Kedem-Katchalsky equations represent a good model for these phenomena [18]. According to these equations, the flux of chemicals per unit surface across the capillary walls is:

$$J_c(p_t, p_v, c_t, c_v) := (1-\sigma)J_b(p_t, p_v)c_{t/v} + P(c_v - c_t) \quad \text{on } \Gamma,$$

where P is the permeability of the vessel wall with respect to solutes, J_b is defined in (1) and σ is the osmotic reflection coefficient. It quantifies the departure of the membrane behavior from the case of ideal permeability. The symbol $c_{t/v}$ denotes the average concentration within the capillary walls. It is defined as a suitable combination of the concentrations on the two sides of the walls [28]. In particular, we set $c_{t/v} := w\overline{c}_t + (1-w)c_v$ where $0 < w < 1$ is a weight that depends on the Péclét number of the solute transport through the wall. Then, under the assumption that capillaries can be modeled as cylindrical channels, the magnitude of the mass flux exchanged per unit length between the network of capillaries and the interstitial volume at each point of the capillary vessels is the following,

$$f_c(\overline{p}_t, p_v, \overline{c}_t, c_v) = 2\pi R\big[(1-\sigma)J_b(\overline{p}_t, p_v)c_{t/v} + P(c_v - \overline{c}_t)\big].$$

2.1.1 Boundary and initial conditions.

The fluid dynamics and mass transport equations are not complete yet. Before being solved, they must be complemented with boundary conditions on the artificial sections that separate the domains Ω and Λ from the surrounding tissue. We model a sample of tissue that is able to exchange fluid and mass with the exterior. In addition, for the governing equations that depend on time, we need to prescribe the initial conditions of the system. Only the drug transport equations depend on time. The initial drug concentrations will be set to the basal values, equal to zero.

For the prescription of boundary conditions on the capillary network we have to define what are the *inflow* and *outflow* boundaries. As shown in Figure 1 using different colors and arrows, we denote by $\partial\Lambda_{in}$ and $\partial\Lambda_{out}$ the inflow and outflow sections of $\partial\Lambda$ respectively. We regulate the flow by enforcing the values of the blood pressure at the extrema of the capillaries. As a result, we prescribe the

following conditions:

$$p_v = p_0 + \Delta p \text{ on } \partial\Lambda_{in} \quad \text{and} \quad p_v = p_0 \text{ on } \partial\Lambda_{out},$$

where the total pressure drop Δp is computed to ensure that the average blood velocity in the network fits with the measured values in healthy human microvasculature [8]. In order to model the administration of the drug through the vascular system, we assume that a fixed drug concentration, denoted with $c_{v,max}$, is injected in the blood stream for a period of time $t \in (0, T)$. We then enforce

$$c_v = c_{v,max} \text{ if } t \in (0,T),\ c_v = 0 \text{ otherwise, on } \partial\Lambda_{in} \quad \text{and} \quad \partial_s c_v = 0 \text{ on } \partial\Lambda_{out}.$$

On the outflow boundary of the network we constrain the derivatives of the drug concentration, rather than the value itself. As a consequence, the concentration value is determined by the model, on the basis of the convection and reaction mechanisms.

The interstitial tissue, Ω, is assumed to be an isotropic material. To comply with this property, we enforce on all the artificial interfaces of the tissue, $\partial\Omega$, boundary conditions that mimic the resistance of the surrounding material. For the fluid dynamics equations, these conditions are discussed in detail in [8] and read as follows:

$$-\kappa_t \nabla p_t \cdot \mathbf{n} = \beta_b (p_t - p_0) \tag{4}$$

where $\mathbf{n}$ is the outer unit normal vector of the interstitial boundary, p_0 is the basal (atmospheric) pressure and β_b is a parameter inversely proportional to the resistance of the surrounding tissue. Equation (4) is very general. When $\beta_b \to 0$ it corresponds to infinite resistance. In this case the fluid flow can not cross the boundaries of Ω. Conversely, large values of β_b (asymptotically $\beta_b \to \infty$) correspond to enforcing $p_t = p_0$ on the boundaries. The sensitivity of the solution with respect to β_b and suitable expressions to calculate it on the basis of the other model parameters are provided in [8]. We proceed analogously for the transport of solutes by setting,

$$-D_t \nabla c_t \cdot \mathbf{n} = \beta_c c_t$$

where β_c quantifies the permeability of the outer tissue with respect to solute transport. Here, we have implicitly assumed that the basal solute concentration is equal to zero. The values of β_b, β_c used in the simulations are reported in Tables 1, 2, respectively.

2.2 Coupled system of O_2 and tirapazamine

Hypoxia targeted drugs, such as *tirapazamine* (TPZ), are designed to be metabolised more quickly by hypoxic cells. The distribution of such drugs in the interstitial tissue then depends on the local availability of oxygen. Mathematical models

and simulations have already been applied to study these effects [21]. The objective of this section is to adapt the single-specie mass transport model developed above to the case of multiple solutes, in order to reproduce the study presented in [21], with a more detailed mathematical description.

We study the distribution of the oxygen partial pressure, denoted by c^{ox}. Since oxygen is persistently supplied by the capillary bed, we rely on the steady problem formulation. Oxygen distributes into the interstitial volume thanks to diffusion and transport. The rate of oxygen absorption depends in turn on the oxygen partial pressure profile itself. This dependence is represented by a Michaelis-Menten formula [18],

$$m^{ox}(c_t^{ox}) = \frac{m_0^{ox}}{c_t^{ox} + c_0^{ox}}$$

where m_0^{ox} represents the maximal oxygen demand, i.e. the rate of oxygen consumption when oxygen is not limited, and c_0^{ox} is the oxygen concentration at which the reaction rate is half of m_0^{ox}. Let us now denote by c^{tpz} the concentration of TPZ. This is a relatively small molecule that obeys to the governing equations of mass transport described in (3a). Following [21] the consumption rate of TPZ depends on the oxygen concentration through the following expression

$$m^{tpz}(c_t^{ox}) = m_0^{tpz} \frac{c_0^{tpz}}{c_0^{tpz} + c_t^{ox}},$$

where m_0^{tpz} is the metabolization rate when TPZ metabolism is not limited by the oxygen concentration, and c_0^{tpz} is the oxygen concentration at which the consumption rate for TPZ is halved compared to that under anoxia. According to Table 2, the dimensions of the metabolization kinetic terms $m^{ox}(c_t^{ox})$ and $m^{tpz}(c_t^{ox})$ are $[time]^{-1}$, which make them match with the other terms of equations (5a) and (5b), respectively.

The general mass transport model (3), adapted to the previous assumptions, ends up with the following equations,

$$
\begin{cases}
\dfrac{\partial c_t^{ox}}{\partial t} + \nabla\cdot(c_t^{ox}\mathbf{u}_t - D_t^{ox}\nabla c_t^{ox}) + m^{ox}(c_t^{ox})c_t^{ox} + \\
\qquad + L_p^{LF}\dfrac{S}{V}(p_t - p_L)c_t^{ox} = f_c^{ox}(\overline{p}_t, p_v, \overline{c}_t^{ox}, c_v^{ox})\delta_\Lambda \qquad \text{in } \Omega \qquad (5a) \\
\dfrac{\partial c_t^{tpz}}{\partial t} + \nabla\cdot(c_t^{tpz}\mathbf{u}_t - D_t^{tpz}\nabla c_t^{tpz}) + m^{tpz}(c_t^{ox})c_t^{tpz} + \\
\qquad + L_p^{LF}\dfrac{S}{V}(p_t - p_L)c_t^{tpz} = f_c^{tpz}(\overline{p}_t, p_v, \overline{c}_t^{tpz}, c_v^{tpz})\delta_\Lambda \qquad \text{in } \Omega \qquad (5b) \\
\dfrac{\partial c_v^{ox}}{\partial t} + \dfrac{\partial}{\partial s}(|\mathbf{u}_v|c_v^{ox} - D_v^{ox}\dfrac{\partial}{\partial s}c_v^{ox}) = \\
\qquad = -\dfrac{1}{\pi R^2}f_c^{ox}(\overline{p}_t, p_v, \overline{c}_t^{ox}, c_v^{ox}) \qquad \text{on } \Lambda \qquad (5c) \\
\dfrac{\partial c_v^{tpz}}{\partial t} + \dfrac{\partial}{\partial s}(|\mathbf{u}_v|c_v^{tpz} - D_v^{tpz}\dfrac{\partial}{\partial s}c_v^{tpz}) = \\
\qquad = -\dfrac{1}{\pi R^2}f_c^{tpz}(\overline{p}_t, p_v, \overline{c}_t^{tpz}, c_v^{tpz}) \qquad \text{in } \Lambda \qquad (5d)
\end{cases}
$$

$$
f_c^*(\overline{p}_t, p_v, \overline{c}_t^*, c_v^*) = 2\pi R\big[(1-\sigma^*)L_p\big((p_v - \overline{p}_t) - \sigma(\pi_v^* - \overline{\pi}_t^*)\big)c_{t/v} + P^*(c_v^* - \overline{c}_t^*)\big]
$$

2.2.1 Parameters of the model and dimensional analysis.

We apply the coupled oxygen-TPZ model, namely equations (5a)-(5d), to calculate the time and space dependent concentration profiles of TPZ in the interstitial volume, after a bolus injection of TPZ equal to C_{max}^{tpz} for a duration of $T_{max} = 20$ minutes. More precisely, we enforce the boundary condition $c_v^{tpz} = C_{max}^{tpz}$ on $\partial\Lambda_{in}$ for $t \in (0, T_{max})$. The numerical simulation is however extended for a longer time interval. The parameters needed to feed the fluid dynamics and the mass transport equations are taken from different sources. For the fluid equations we refer to [8] and references therein. For the transport of oxygen and TPZ we use the dataset provided in [21]. The parameters that will be used in the numerical simulations (and the corresponding sources) are reported in Table 1.

Before proceeding, we aim to use the available data to verify the assumption that the contribution of oxygen and TPZ to the oncotic pressure is negligible. This hypothesis has already been widely investigated for oxygen, [28, 26], and it results to be accurately satisfied, because oxygen is a very small molecule. For TPZ the question remains open. An upper bound for the oncotic pressure generated by TPZ dissolved in blood is $\pi_{max}^{tpz} = \sigma^{tpz}R_gTC_{max}^{tpz}$. The main issue is the quantification of the reflection coefficient σ^{tpz}. According to [11, 18, 28], this parameter can be estimated as

$$
\sigma^{tpz} = \Big(1 - \big(1 - \frac{r^{tpz}}{r^{pores}}\big)^2\Big)^2 \quad \text{and} \quad r^{tpz} = \frac{k_BT}{6\pi\mu D^{tpz}}
$$

parameter	units	value	source
$p_0 + \Delta p$	mmHg	35	[18]
Δp	mmHg	1.25	[8]
$\sigma\pi_v$	mmHg	28	[18]
$\sigma\pi_t$	mmHg	0.1	[18]
L_p	$\mathrm{m^2 s/kg}$	10^{-10}	[23]
$L_p^{LF}\frac{S}{V}$	$\mathrm{mmHg^{-1}\ hours^{-1}}$	0.5	[3]
β_b	–	10^{-6}	[8]

Table 1: Physical parameters characterizing the perfusion problem.

parameter	units	oxygen		TPZ	
D_t	cm^2/s	1.35×10^{-5}	[21]	1.87×10^{-6}	[21]
D_v	cm^2/s	1.35×10^{-3}	$--$	1.87×10^{-4}	$--$
P	cm/s	3.5×10^{-3}	[33]	5×10^{-3}	$--$
m_0^{tpz}	s^{-1}			0.0317	[21]
m_0^{ox}	$mmHg/s$	8.0645	[21]		
C_{max}^{tpz}	g/m^3			48	[21]
C_{max}^{ox}	$mmHg$	100	[32]		
β_c	–	10^{-3}	[8]	10^{-3}	[8]

Table 2: Physical parameters for oxygen and TPZ delivery, transport and metabolization.

where r^{tpz} is an estimate of the TPZ molecular radius and r^{pores} quantifies the average dimension of the endothelial fenestrations in the capillary walls. For the latter, following [28] and references therein, we take $r^{pores} = 5 \times 10^{-9}$ m. For the former, we use the Stokes-Einstein equation (i.e the formula for r^{tpz} reported above, where $k_B T$ is the Boltzmann thermal energy and μ is the viscosity of blood plasma) to approximate the TPZ radius using the molecule diffusivities, provided in Table 1. This results in the following upper bound for the TPZ radius $r^{tpz} < 3 \times 10^{-10}$ m. When we compare this estimate with the Bohr radius (the most probable distance between the proton and electron in a hydrogen atom), it turns out that one TPZ molecule should span approximately over 5 radii, which seems to be appropriate for the molecule, whose chemical formula is $C_7H_6N_4O_2$. Using the available estimate for r^{tpz} we obtain $\sigma^{tpz} < 0.013$, which completely justifies our assumption. Indeed, the corresponding oncotic pressure is $\pi_{max}^{tpz} = \sigma^{tpz} R_g T C_{max}^{tpz} < 0.08$ mmHg. This value is almost negligible with respect to the oncotic pressure gradient induced by the blood proteins that amounts to 25 mmHg.

Given the set of parameters, our first step towards the application of the models is to perform a dimensional analysis of the corresponding equations. The

results will inform us on the relative magnitude of the concurrent phenomena that affect mass transport, such as molecular diffusion, convection and ligand-receptor interactions. We choose length, velocity and concentration as primary variables for the analysis. The characteristic length, $d = 50\mu m$, is the average spacing between capillary vessels, the characteristic velocity, $U = 100\mu m/s$, is the average velocity in the capillary bed, $\delta P = 1$ mmHg is the characteristic hydrostatic pressure drop along the extrema of the capillary network that will be considered in the simulations and the characteristic concentration, C_{max} (Table 1), is defined as the maximal admissible value at the systemic level for each considered chemical specie. The dimensionless form of the mass transport problem is then,

$$\begin{cases} \dfrac{\partial c_t^*}{\partial t} + \nabla \cdot (c_t^* \mathbf{u}_t - A_t^* \nabla c_t^*) + Da_t^*(c_t^{ox}) c_t^* + Q_{PL}(p_t - p_L) c_t^* \\ \qquad\qquad = f_c^*(p_t, p_v, c_t^*, c_v^*)\delta_\Lambda \qquad \text{in } \Omega \\ \dfrac{\partial c_v^*}{\partial t} + \dfrac{\partial}{\partial s}(|\mathbf{u}_v| c_v^* - A_v^* \dfrac{\partial}{\partial s} c_v^*) = -\dfrac{d^2}{\pi R^2} f_c^*(p_t, p_v, c_t^*, c_v^*) \qquad \text{in } \Lambda \end{cases}$$

$$f_c^*(p_t, p_v, c_t^*, c_v^*) = 2\pi(R/d)\big[(1-\sigma^*)Q\big((p_v - \overline{p}_t) - \sigma(\pi_v - \overline{\pi}_t)\big)c_{t/v}^* + \Upsilon^*(c_v^* - \overline{c}_t^*)\big]$$

where all the symbols now refer to dimensionless quantities and the superscript $*$ stands for either oxygen (ox) or tirapazamine (tpz). For convenience, we do not differentiate the notation from the dimensional setting. The dimensionless groups that characterize the flow are

$$u_t = \frac{|\mathbf{u}_t|}{U}, \;\; u_v = \frac{|\mathbf{u}_v|}{U}, \;\; Q = \frac{L_p \delta P}{U}, \;\; Q_{PL} = L_p^{LF} \frac{S}{V} \frac{\delta P d}{U}.$$

We refer to [8] for a detailed discussion of their interplay. Here, we are particularly interested in the analysis of mass transport, which is described by the following quantities:

$$A_v^* = \frac{D_v^*}{dU}, \;\; A_t^* = \frac{D_t^*}{dU}, \;\; Da_t^* = m^* \frac{d}{U}, \;\; \Upsilon^* = \frac{P^*}{U}$$

The groups A_t^*, A_v^* are the inverse of the Péclét numbers in the interstitium and the blood stream, respectively. They quantify the ratio of diffusion and transport phenomena. The Damkohler number, Da_t^*, represents the magnitude of metabolism with respect to diffusion. Finally, Υ^* characterizes the magnitude of leakage from the capillary bed. Using the parameters reported in Table 2, the magnitude of the dimensionless groups for oxygen and TPZ, respectively, is

$$A_v^{ox} = 100, \;\; A_t^{ox} = 0.27, \;\; Da_t^{ox} = 4.0323, \;\; \Upsilon^{ox} = 0.364$$

$$A_v^{tpz} = 7, \;\; A_t^{tpz} = 0.0187, \;\; Da_t^{tpz} = 0.0159, \;\; \Upsilon^{tpz} = 0.52$$

where to quantify the reaction coefficients Da_t^{ox} and Da_t^{tpz}, we take maximal oxygen concentration, i.e. $C^{ox} = 100$ mmHg.

We observe that $A_v^{ox} > A_v^{tpz} > 1 > A_t^{ox} > A_t^{tpz}$. Since the molecular diffusivity of oxygen and TPZ in the interstitial tissue is rather low, the dynamics of these molecules in the interstitium is moderately transport dominated. We notice, however, that this conclusion is based on the mean blood velocity in the capillaries, U, used to quantify transport. It could thus lead to a slight overestimation of the transport phenomena in the tissue.

Concerning the Damkohler numbers, we notice that $Da_t^{ox} > A_t^{ox}$, which means that the distribution of oxygen in the tissue is reaction dominated, while for TPZ these two mechanisms are almost in equilibrium, i.e. $Da_t^{tpz} \simeq A_t^{tpz}$.

2.3 Transport of nanoparticles and drug delivery

Nanoparticles are used as vectors for the delivery of drugs to the tumor tissue. The advantage of this technology with respect to systemic delivery is that chemoterapic agents are released selectively to the tumor mass [19]. The side effects of drugs on patients health are thus reduced. We aim at modeling the transport of nanoparticles in the capillary network and the consequent delivery of a drug, which in our case is again TPZ, to enable comparisons with the bolus injection delivery method. A large variety of cancer treatment methods based on nanoparticle delivery is available or under development [37]. Thanks to its generality, the computational model could be adapted to describe many of them. Here, we focus on modeling drug delivery from particles designed to travel the vascular network and selectively interact with particular receptors on the capillary walls. Mathematical models describing these phenomena have been recently proposed, we refer to [17, 22]. They are based on similar concepts. In the former study, nanoparticle adhesion to tumor vasculature is addressed. The latter one is devoted to study the interaction of nanoparticles with the coronary arteries, in presence of regions affected by inflammation. Our model arises from the general equations of blood flow and mass transport, with some modifications. In particular, it has to be adapted to account for three different stages of the delivery process: (*i*) the transport of nanoparticles in the capillary network; (*ii*) the adhesion of the particles to the capillary wall, adopting the framework proposed in [17, 22]; (*iii*) the delivery of the encapsulated drug to the surrounding tissue. Given the moderately short time scales addressed in the forthcoming numerical examples, as well as the complexity of the biological phenomena involved, many of which are not completely understood yet, we do not consider modeling of nanoparticles extravasation and migration into the interstitial volume.

Steps (i) & (ii): nanoparticle transport and adhesion. The model accounting for nanoparticle transport in the blood stream and their adhesion to the wall results in the following equations:

$$\frac{\partial c_v}{\partial t} + \frac{\partial}{\partial s}(|\mathbf{u}_v| c_v - D_v \frac{\partial c_v}{\partial s}) + \frac{2\pi R}{\pi R^2} \Pi c_v = 0 \quad \text{in } \Lambda \times (0, T)$$

where $c_v(\mathbf{x}, t)$ is the nanoparticle concentration inside the vessels and it is measured as number of particles per unit volume [$\sharp/\mathrm{m}^3$]. The adhesion of particles to the wall, that was not accounted in the general model, is described as a sink term distributed along the length of the capillary network, namely Πc_v on Λ. The new term Πc_v is a flux of particles sequestrated to the flow per unit surface of capillary wall. Since we consider a one-dimensional model along the capillary axis, we use the corresponding flux per unit length $2\pi R \Pi c_v$. The sink term, per unit volume, equivalent to this flux is then obtained by scaling the flux per unit length with the vessel cross section, that is πR^2. The vascular deposition parameter, Π, is estimated using a ligand-receptor model for the interaction of particles with the endothelial layer. In particular, we use the model setting of [22]. For the sake of completeness, we report here the main components of the model. The vascular deposition parameter is defined as

$$\Pi(s) = P_a |S(s)| \frac{d_p}{2}$$

where P_a is the probability of particle adhesion, $S(s)$ is the the wall shear rate and d_p is the diameter of the considered nanoparticles. Given the plasma viscosity μ, the wall shear stress at the axial coordinate s along the capillary network is $\mu S(s)$. As a result, we compute the wall shear rate using the Poiseuille's flow equation. To this aim, we remind that the network Λ can be decomposed into individual branches Λ_i, $i = 1, \ldots, N$. Then, the shear rate assumes a constant value on each branch given by

$$|S_i| = \frac{R}{2\mu} \frac{|\Delta_i p_v|}{L_i}$$

where $|\Delta_i p_v|$ is the absolute value of the pressure drop along each branch of the network and L_i is the branch length. The probability of adhesion, P_a, is in turn defined as a function of particle size, shape and surface properties,

$$P_a(s) = m_l K_a^0 \alpha_2 \pi r_0^2 exp\bigg(- \beta \frac{\mu |S(s)|}{\alpha_2} \bigg).$$

In the above expression m_l is the surface density of the ligand molecules that decorate the nanoparticle surface and K_a^0 is the affinity constant of the interaction between ligands and receptors. The parameter α_2, defined as

$$\alpha_2 = m_r \bigg[1 - \bigg(1 - \frac{\Delta}{d_p/2} \bigg)^2 \bigg]$$

is a function of the density of receptors on the endothelial surface, m_r, and of the separation distance between the particle and the substrate at the equilibrium, Δ. The parameter r_0 represents the radius of the adhesion point and $\beta = \frac{\lambda 6F}{k_B T}$ is a constant, where F is the coefficient of hydrodynamic drug force on the spherical particle and $k_B T$ is the Boltzmann thermal energy.

The model must be complemented by suitable initial and boundary conditions. At the inlet $\partial\Lambda_{in}$ we prescribe a Dirichlet boundary condition c_v^0, which represents the amount of injected particles. At the outflow $\partial\Lambda_{out}$ we specify a homogeneous Neumann boundary condition. We assume that the blood stream does not contain any particle at the initial time.

Once the problem for particle transport and adhesion is solved, we compute the density of nanoparticles adhering per unit surface to the wall as

$$\Psi(s,t) := \int_0^t \Pi(s) c_v(s,\tau) d\tau.$$

Step (iii): drug release from nanoparticles. The particles decorating the capillary wall are loaded with drug and they are able to release it to the surrounding tissue. Observing that the particles are in direct contact with the capillary wall, we assume that the drug release rate to the interstitial volume per unit capillary surface is determined by the combination of the flux delivered by a single particle with the density of particles adhering to the wall. Determining the release profile of a single (spherical) loaded particle is a well studied problem in pharmacology [24]. Here, following [24, 1, 27] we define it using a power law model,

$$\frac{q(t)}{q_\infty} = \frac{t^b}{t^b + m}, \quad q_\infty = c_{np}^* V_{np}, \quad \text{then} \quad q(t) = \frac{t^b}{t^b + m} c_{np}^* V_{np},$$

where $q(t)$ is the amount of drug released and q_∞ is the total drug load of a nanoparticle, given by the total drug concentration inside the nanoparticle, c_{np}^* (where $*$ denotes an unspecified drug loaded on the particles), multiplied by the nanoparticle volume V_{np}. The parameter m is expressed in dimensions of $[time]^b$. The two parameters m and b reflect the structural and geometric properties of the delivery system. The drug release rate from a single nanoparticle is therefore obtained as

$$J_{np}(t) = \frac{dq(t)}{dt} = \frac{m \cdot b \cdot t^{b-1}}{(t^b + m)^2} c_{np}^* V_{np},$$

and the total drug release rate per unit surface is computed as,

$$J(s,t) = J_{np}(t)\Psi(s,t).$$

To conclude, we apply the immersed boundary method to describe the capillary bed as a source term concentrated on the centerline Λ. More precisely, the action of drug loaded nanoparticles on the interstitial tissue is described by the source term $2\pi R J(s,t)$, assuming that the capillaries are cylindrical channels of radius R. To compare the nanoparticle delivery approach with the bolus delivery strategy previously considered, we load the particles with TPZ. The drug concentration into the tissue is modeled by the following equations:

parameter	units	value
β	N^{-1}	$2.39\ \times 10^{11}$
μ	$\mathrm{Ns/m}^2$	0.001
d_p	m	$2\ \times 10^{-6}$
α_2	$\sharp/\mathrm{m}^2$	$3.4\ \times 10^{9}$
$m_l K_a^0 r_0^2$	m^2	$1.2585\ \times 10^{-9}$
b	–	0.8
m	hours^b	1
C_{max}^{np}	$\sharp/\mathrm{m}^3$	1.4354×10^{12}
D_v	cm^2/s	6.98×10^{-9}

Table 3: Physical parameters used to model nanoparticle injection and adhesion [22].

$$\begin{cases} \dfrac{\partial c_t^{tpz}}{\partial t} + \nabla \cdot (c_t^{tpz}\mathbf{u}_t - D_t^{tpz}\nabla c_t^{tpz}) + m^{tpz}(c_t^{ox})c_t^{tpz} \\ \qquad + L_p^{LF}\frac{S}{V}(p_t - p_L)c_t^{tpz} = 2\pi R J(t)\delta_\Lambda & \text{in } \Omega \times (0,T] \quad (6a) \\ \\ D_t^{tpz}\nabla c_t^{tpz}\cdot \mathbf{n} = \beta_c(c_t^{tpz} - c_0^{tpz}) & \text{on } \partial\Omega \times (0,T] \quad (6b) \end{cases}$$

2.3.1 Parameters of the model.

The nanoparticle transport and adhesion model requires to characterize several parameters, for which we refer to Table 1 in [22]. Furthermore, it is possible to calibrate the power law model in order to describe different scenarios, for example a fast release mechanism or a slow release rate. We fix the parameters of the model, m and b, such that 90% of the total drug is released within one day. The parameter values characterizing particle adhesion and drug release are reported in Table 3.

Another important quantity is the concentration of nanoparticles injected at the inflow of capillary network. Since we are interested in comparing the amount of TPZ delivered from bolus and nanoparticle injection, we aim at determining the concentration of injected nanoparticles that match the TPZ bolus concentration, previously defined as C_{max}^{tpz}. Similarly, the concentration of injected nanoparticles will be denoted by C_{max}^{np} and its value is determined according to the following balance equation,

$$C_{max}^{np} c_{np}^{tpz} V_{np} = C_{max}^{tpz}.$$

To determine the value of C_{max}^{np} we need an estimate of the amount of drug cast in each particle, namely c_{np}^{tpz}. To determine this value we rely on two assumptions: (i) the drug mass fraction in each particle, denoted as f^{tpz}, is equal to the unity;

(ii) the density of the particles is comparable to the density of water, ρ_w. As a result, we conclude that

$$c_{np}^{tpz} = \rho_w f^{tpz}.$$

and we compute the value of C_{max}^{mp} that is reported in Table 3.

2.4 Computational methods

For complex geometrical configurations explicit solutions of problems (2), (5) and (6) are not available. Numerical simulations are the only way of applying the model to real cases. The discretization of the flow problem (2) is described in [8] and it is achieved by means of the finite element method that arises from the variational formulation of the problem combined with a partition of the domain into small elements. We follow the same method also to discretize problems (5) and (6). More precisely, starting from the problems of oxygen and TPZ mass transport, we multiply each tissue equation in (5) for a test function $q_t \in V_t = H^1_\alpha(\Omega)$, where $H^1_\alpha(\Omega)$ with $\alpha \in (0,1)$ is the natural trial space for the problem in the interstitium, as discussed in [8] and references therein. We integrate over Ω and the transport operator is treated using integration by parts combined, for the sake of simplicity, with homogeneous Neumann conditions on $\partial\Omega$. Regarding the interface flux term we write

$$\big(f_c^*(p_t, p_v, c_t^*, c_v^*)\delta_\Lambda, q_t\big)_\Omega = \big(f_c^*(p_t, p_v, c_t^*, c_v^*), q_t\big)_\Lambda.$$

We proceed similarly for the governing equation on the capillary bed. Integrating by parts on each branch Λ_i separately, it is possible to manipulate the resulting equations in order to naturally impose the mass conservation at each node of the network, see [8] for details. This property is satisfied provided that the test functions of the pressure field on the capillary bed are continuous on the entire network, namely $q_v \in C^0(\Lambda)$. In particular we choose $V_{v,0}$ as the subspace of $H^1(\Lambda)$ of functions which vanish on the boundaries of Λ and therefore $V_{v,0} \subset C^0(\Lambda)$ on 1D manifolds. This allows us to obtain

$$\big(\frac{\partial c_v^*}{\partial t}, q_v\big)_\Lambda + \big(|\mathbf{u}_v| c_v^* - D_v^* \frac{\partial}{\partial s} c_v^*, \frac{\partial}{\partial s} q_v\big)_\Lambda = \big(-\frac{1}{\pi R^2} f_c^*(p_t, p_v, c_t^*, c_v^*), q_v\big)_\Lambda, \ \forall q_v \in V_{v,0}.$$

Then the weak formulation of (5) requires to find $c_t^* \in V_t$ and $c_v^* \in V_{v,0}$ with $* = ox$, tpz such that,

$$\begin{cases} \big(\frac{\partial c_t^*}{\partial t}, q_t\big)_\Omega + a_t(c_t^*, q_t) + b_\Lambda^t(\overline{c}_t^*, q_t) = b_\Lambda^t(c_v^*, q_t), \ \forall q_t \in V_t, & \text{(7a)} \\ \big(\frac{\partial c_v^*}{\partial t}, q_v\big)_\Lambda + a_v(c_v^*, q_v) + b_\Lambda^v(c_v^*, q_v) = b_\Lambda^v(\overline{c}_t^*, q_v), \ \forall q_v \in V_{v,0}, & \text{(7b)} \end{cases}$$

with the following bilinear forms,

$$
\begin{aligned}
a_t(c_t^*, q_t) &:= \big(c_t^* \mathbf{u}_t - D_t^* \nabla c_t^*, \nabla q_t\big)_\Omega + \big(m^*(c_t^{ox}) c_t^*, q_t\big)_\Omega + L_p^{LF} \tfrac{S}{V} \big((p_t - p_L) c_t^*, q_t\big)_\Omega, \\
a_v(c_v^*, q_v) &:= \big(|\mathbf{u}_v| c_v^* - D_v^* \frac{\partial}{\partial s} c_v^*, \frac{\partial}{\partial s} q_v\big)_\Lambda, \\
b_\Lambda^t(c_v^*, q_v) &:= \big(2\pi R\big[(1-\sigma^*) L_p\big((p_v - \overline{p}_t) - \sigma(\pi_v - \overline{\pi}_t)\big)(1-w) c_v^* + P^* c_v^*\big], q_v\big)_\Lambda, \\
b_\Lambda^t(\overline{c}_t^*, q_t) &:= \big(2\pi R\big[(1-\sigma^*) L_p\big((p_v - \overline{p}_t) - \sigma(\pi_v - \overline{\pi}_t)\big) w \overline{c}_t^* - P^* \overline{c}_t^*\big], q_t\big)_\Lambda, \\
b_\Lambda^v(c_v^*, q_v) &:= \big(2/R\big[(1-\sigma^*) L_p\big((p_v - \overline{p}_t) - \sigma(\pi_v - \overline{\pi}_t)\big)(1-w) c_v^* + P^* c_v^*\big], q_v\big)_\Lambda, \\
b_\Lambda^v(\overline{c}_t^*, q_t) &:= \big(2/R\big[(1-\sigma^*) L_p\big((p_v - \overline{p}_t) - \sigma(\pi_v - \overline{\pi}_t)\big) w \overline{c}_t^* - P^* \overline{c}_t^*\big], q_t\big)_\Lambda.
\end{aligned}
$$

We proceed in a similar way also for equations (6). The variational problem for nanoparticle transport and TPZ delivery requires to find $c_t^{tpz} \in V_t$ and $c_v \in V_{v,0}$ such that

$$
\begin{cases}
\big(\frac{\partial c_t^{tpz}}{\partial t}, q_t\big)_\Omega + a_t^{tpz}(c_t^{tpz}, q_t) = F(t), \ \forall q_t \in V_t, & \text{(8a)} \\
\big(\frac{\partial c_v}{\partial t}, q_v\big)_\Lambda + a_v^{tpz}(c_v, q_v) = 0, \ \forall q_v \in V_{v,0}, & \text{(8b)}
\end{cases}
$$

and the bilinear forms are,

$$
\begin{aligned}
a_t^{tpz}(c_t^{tpz}, q_t) &:= \big(c_t^{tpz} \mathbf{u}_t - D_t^{tpz} \nabla c_t^{tpz}, \nabla q_t\big)_\Omega + \big(m^{tpz}(c_t^{ox}) c_t^{tpz}, q_t\big)_\Omega + \big(L_p^{LF} \tfrac{S}{V} (p_t - p_L) c_t^{tpz}, q_t\big)_\Omega, \\
a_v^{tpz}(c_v, q_v) &:= \big(|\mathbf{u}_v| c_v - D_v \frac{\partial c_v}{\partial s}, \frac{\partial}{\partial s} q_v\big)_\Lambda + \big(\frac{2\pi R}{\pi R^2} \Pi c_v, q_v\big)_\Lambda, \\
F(t) &:= \big(2\pi R J(t), q_t\big)_\Lambda.
\end{aligned}
$$

For the spatial approximation we first introduce an admissible family of partitions of Ω into tetrahedrons $K \in \mathcal{T}_t^h$, where the apex h denotes the mesh characteristic size. For the discretization of the capillary bed, each branch Λ_i is partitioned into a sufficiently large number of linear segments E, whose collection is Λ_i^h, which represents a finite element mesh on a one-dimensional manifold. Let $\Lambda^h := \cup_{i=1}^N \Lambda_i^h$ be the finite element partition of the entire capillary bed. At the discrete level, one of the advantages of our problem formulation is that the partition of the domains Ω and Λ into elements are completely independent. The computational meshes used to solve the transport problems are reported in Figure 2.

Let $V_t^h := \{v \in C^0(\Omega) : \ v|_K \in \mathbb{P}^1(K), \ \forall K \in \mathcal{T}_t^h\}$ be the space of piecewise linear continuous finite elements on $\mathcal{T}_t^h$ and let $V_{v,i}^h := \{v \in C^0(\Lambda_i) : \ v|_E \in \mathbb{P}^1(E), \ \forall E \in \Lambda_i^h\}$ be the piecewise linear and continuous finite element space on Λ_i. The numerical approximation of the equation posed on the capillary bed is then achieved using the space $V_v^h := \big(\cup_{i=1}^N V_{v,i}^h\big) \cap C^0(\Lambda)$. The discrete problems arising from (7) and (8) require to find $c_t^{*h} \in V_t^h$, $c_v^{*h} \in V_{v,0}^h$ and $c_t^{tpz,h} \in V_t^h$ and

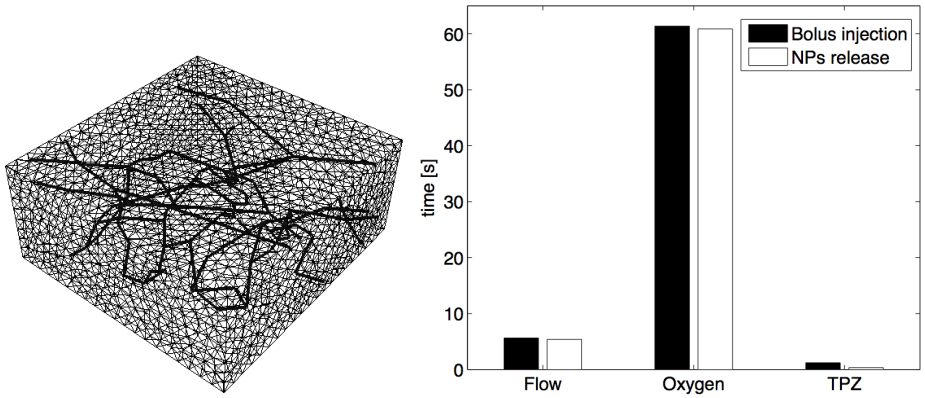

Figure 2: On the left: meshes used to solve problems (10), (11) and (12). The partition of the domains Ω and Λ into elements are completely independent. In particular the partition of Ω is composed by 32624 elements, while the partition of Λ is composed by 8400 nodes, 80 nodes for each branch. On the right: computational time for solving the algebraic systems of the flow equations, the oxygen transport problem and the TPZ mass transport problem for the two different modalities of transport. We represent one single time step for the solution of the TPZ transport problem. The bars quantify the CPU time measured in seconds.

$c_v^h \in V_{v,0}^h$ such that

$$\begin{cases} (\dfrac{\partial c_t^{*h}}{\partial t}, q_t^h)_\Omega + a_t(c_t^{*h}, q_t^h) + b_{\Lambda^h}^t(\overline{c}_t^{*h}, q_t^h) = b_{\Lambda^h}^t(c_v^{*h}, q_t^h), \ \forall q_t^h \in V_t^h, & \text{(9a)} \\ \\ (\dfrac{\partial c_v^{*h}}{\partial t}, q_v^h)_\Lambda + a_v(c_v^{*h}, q_v^h) + b_{\Lambda^h}^v(c_v^{*h}, q_v^h) = b_{\Lambda^h}^v(\overline{c}_t^{*h}, q_v^h), \ \forall q_v^h \in V_{v,0}^h, & \text{(9b)} \end{cases}$$

$$\begin{cases} (\dfrac{\partial c_t^{tpz,h}}{\partial t}, q_t^h)_\Omega + a_t^{tpz}(c_t^{tpz,h}, q_t^h) = F(t), \qquad \forall q_t^h \in V_t^h, & \text{(10a)} \\ \\ (\dfrac{\partial c_v^h}{\partial t}, q_v^h)_\Lambda + a_v^{tpz}(c_v^h, q_v^h) = 0, \qquad \forall q_v^h \in V_{v,0}^h, & \text{(10b)} \end{cases}$$

where the bilinear forms $a_t(\cdot,\cdot)$, $a_v(\cdot,\cdot)$, $b_{\Lambda^h}(\cdot,\cdot)$, $a_t^{tpz}(\cdot,\cdot)$, $a_v^{tpz}(\cdot,\cdot)$ are the same as before, with the only difference that $b_{\Lambda^h}(\cdot,\cdot)$ is now defined over the discrete representation of the network Λ_h. The interpolation and average operators, that are need to evaluate the bilinear form $b_{\Lambda^h}(\cdot,\cdot)$, are described in [8] and the error analysis of the present scheme can be addressed with the tools provided in [13].

The space discretization must be complemented with a time advancing scheme. For the numerical approximation of the variational problems (9) and (10), we consider a standard backward Euler time advancing method. Let $\Delta t > 0$ be the time step, $t_n = n\Delta t$ the n-th time point, and $c_t^{*h,n} \in V_t^h$, $c_v^{*h,n} \in V_{v,0}^h$, the numerical approximations of $c_t^{*h}(t_n)$ and $c_v^{*h}(t_n)$. As a result, we obtain the

following discrete problems: given $c_t^{*h,n} \in V_t^h$ and $c_v^{*h,n} \in V_{v,0}^h$ find $c_t^{*h,n+1} \in V_t^h$ and $c_v^{*h,n+1} \in V_{v,0}^h$, such that

$$\begin{cases} \big(\frac{1}{\Delta t} c_t^{*h,n+1}, q_t^h\big)_\Omega + a_t(c_t^{*h,n+1}, q_t^h) + b_{\Lambda^h}^t(\overline{c}_t^{*h,n+1}, q_t^h) \\ \qquad = \big(\frac{1}{\Delta t} c_t^{*h,n}, q_t^h\big)_\Omega + b_{\Lambda^h}^t(c_v^{*h,n+1}, q_t^h),\ \forall q_t^h \in V_t^h, \end{cases} \tag{11a}$$

$$\begin{cases} \big(\frac{1}{\Delta t} c_v^{*h,n+1}, q_v^h\big)_\Lambda + a_v(c_v^{*h,n+1}, q_v^h) + b_{\Lambda^h}^v(c_v^{*h,n+1}, q_v^h) \\ \qquad = \big(\frac{1}{\Delta t} c_v^{*h,n}, q_v^h\big)_\Lambda + b_{\Lambda^h}^v(\overline{c}_t^{*h,n+1}, q_v^h),\ \forall q_v^h \in V_{v,0}^h, \end{cases} \tag{11b}$$

An equivalent approach is applied to discretize equations (10).

Finally, we observe that the equation which describes the oxygen concentration transport, (5), involves a non linear term, represented by the Michelis-Menten reaction formula. To solve the problem, we apply an iterative scheme strategy, where the oxygen concentration is evalutated at the previous iterative step. For simplicity of notation, to address this iterative scheme we drop the time index $n+1$. This index will be explicitly indicated only when referring to a time step different than t_{n+1}. For the same reason, we drop the index h everywhere. Then, for all $n = 1, \dots, N$ given an initial guess $c_t^{ox,0}$, $c_v^{ox,0}$ and a tolerance ε, the iterative strategy consists to find a sequence $c_t^{ox,k}$, $c_v^{ox,k}$ for $k = 1, 2, \dots$ such that,

$$\begin{cases} \big(\frac{1}{\Delta t} c_t^{ox,k}, q_t\big)_\Omega + \big(c_t^{ox,k}\mathbf{u}_t - D_t^{ox}\nabla c_t^{ox,k}, \nabla q_t\big)_\Omega \\ \qquad + \big(m^{ox}(c_t^{ox,k-1})c_t^{ox,k}, q_t\big)_\Omega + L_p^{LF}\frac{S}{V}\big((p_t - p_L)c_t^{ox,k}, q_t\big)_\Omega \\ \qquad = \big(\frac{1}{\Delta t} c_t^{ox,k,n}, q_t\big)_\Omega - b_{\Lambda^h}^t(\overline{c}_t^{ox,k}, q_t) + b_{\Lambda^h}^t(c_v^{ox,k}, q_t), \forall q_t \in V_t^h, \end{cases} \tag{12a}$$

$$\begin{cases} \big(\frac{1}{\Delta t} c_v^{ox,k}, q_v\big)_\Lambda + a_v(c_v^{ox,k}, q_v) + b_{\Lambda^h}^v(c_v^{ox,k}, q_v) \\ \qquad = \big(\frac{1}{\Delta t} c_v^{ox,k,n}, q_v\big)_\Lambda + b_{\Lambda^h}^v(\overline{c}_t^{ox,k}, q_v),\ \forall q_v \in V_{v,0}^h, \end{cases} \tag{12b}$$

until the following stopping criterion is satisfied:

$$\frac{\|c_t^{ox,k} - c_t^{ox,k-1}\|_0}{\|c_t^{ox,k}\|_0} + \frac{\|c_v^{ox,k} - c_v^{ox,k-1}\|_0}{\|c_v^{ox,k}\|_0} < \varepsilon. \tag{13}$$

where $\|\cdot\|_0$ is the Euclidean norm of the vector of nodal values.
Regarding the coupling between the oxygen and the TPZ concentration, we actually solve the steady counterpart of (11) for the oxygen transport, because oxygen is persistently supplied by the capillary bed. Therefore, once computed the oxygen concentration profile, we use it to determine once for all the reaction

term that appears in the TPZ transport equation. This choice seems to be reasonable also because there isn't any feedback of the TPZ concentration on the oxygen consumption.

	Bolus injection	Nanoparticles release
problems initialization	301.7	301.59
assembling fluid system	1.02	1.04
solving fluid system	5.62	5.39
assembling O_2 system	1.32	1.35
solving O_2 system	61.36	60.86
assembling drug system	1.37	1.48
solving drug system (one single step)	1.2	0.21
solving drug system (T=20 min)	3374.04	1231.24

Table 4: Computational time for solving different parts of problems (10), (11) and (12). Computational time is measured in seconds.

For the numerical solution of problems (12), (11) and (10) we use GetFem++, a general purpose C++ finite element library [30]. The discretization of flow problem (2), already described in [8], is solved applying the GMRES method with incomplete-LU preconditioning. The tolerance for the stopping criterion for the iterative method to solve the oxygen transport equations (12) is fixed to $\varepsilon = 10^{-8}$. We reach the convergence in 61 iterations. At each iteration, we apply the GMRES method to solve the corresponding linear systems. Regarding the TPZ transport, the monolithic algebraic system constructed from (11) is again solved using the GMRES method with incomplete-LU preconditioning. Conversely, the two equations composing system (10) are actually decoupled, therefore they are addressed in sequence: we solve the vessel equation (10b) first, in order to compute the flux $J(t)$, which is the forcing term of the tissue equation (10a). Since these equations are independent, their numerical solution turns out to be faster than the one of system (11), as we observe from the results reported in Figure 2 and in Table 4.

Referring to the dimensional analysis performed in Section 2.2.1, we notice that the Damkohler number for the oxygen transport equation is bigger than the molecular diffusivity in the tissue, namely $Da_t^{ox} > A_t^{ox}$, which means that the distribution of oxygen in the tissue is reaction dominated, while for TPZ these two mechanisms are almost in equilibrium, i.e. $Da_t^{tpz} \simeq A_t^{tpz}$. We also observe that the magnitude of leakage, Υ^*, is always bigger than that of diffusivity in the interstitium, A_t^*. To cope with the reaction dominated nature of these mass transport equations, we adopt the mass lumping stabilization techniques addressed in [29] for the reaction terms corresponding to the coefficients Da_t^{ox} and Υ^*. Although the dimensional analysis addressed in Section 2.2.1 suggests that the mass transport problems in the interstitial tissue may be moderately

transport dominated, numerical experiments confirm that resorting to stabilization methods for the convective terms is not required for the applications that will be addressed.

3 Results and discussion

The delivery of anticancer agents mediated through nanoparticle injection in the blood stream features significant advantages with respect to the traditional drug bolus delivery, because it increases the permanence of drug available in the systemic circulation [37]. We aim to explore the potential of the proposed simulation framework to capture these effects.

3.1 Indicators of drug delivery performance

The concentration profiles in the vessels, $c_v(t,s)$, and in the tissue, $c_t(t,x)$ are the natural outputs of the mass transport model described so far. From the clinical standpoint, these may not be the most significant indicators of the treatment performance. For this reason, we also study the amount of TPZ metabolised by cells up to a given reference time. We denote this quantity as $M^{tpz}(t,x)$. In addition, for more quantitative comparisons, we look at the total amount of TPZ metabolised in the considered portion of tissue, that is $\overline{M}^{tpz}(t)$. On the basis of the Michaelis-Menten metabolization kinetics adopted in equation (5), these indicators are defied as

$$M^{tpz}(t,\boldsymbol{x}) = \int_0^t m^{tpz}\big(c_t^{ox}(\tau,\boldsymbol{x}), c_t^{tpz}(\tau,\boldsymbol{x})\big)d\tau, \quad \overline{M}^{tpz}(t) = \int_\Omega M^{tpz}(t,\boldsymbol{x})d\boldsymbol{x}.$$

Following [21], the amount of drug metabolised in the tissue can be related to the cell survival. In particular, the cell *surviving fraction* (SF) represents the complement of the fraction of cells treated (killed) by TPZ with respect to the number of control cells (the total number of cells in the tissue, before treatment started). Several models are available to quantify the surviving fraction [21]. In particular, we use

$$SF(t,\boldsymbol{x}) = \exp\big(-\alpha M^{tpz}(t,\boldsymbol{x})\big), \quad \overline{SF}(t) = \exp\big(-\alpha \overline{M}^{tpz}(t)\big)$$

where α is a phenomenological coefficient. For the following calculations we assume $\alpha = 2.52 \times 10^{-4}$ $\mu\mathrm{M}^{-1}$ (0.0014 g/m^3) as in [21].

3.2 Oxygen transport and TPZ delivery from bolus injection

We analyze the simulations of oxygen and TPZ transport obtained with model (5). In Figure 3 we compare the oxygen and the TPZ concentrations 20 minutes after that the delivery of TPZ into the systemic circulation has started. Oxygen concentration patterns substantially depend on the density of capillaries per

unit volume. Regions of the sample tissue not well perfused by the capillary network show low oxygen concentrations, justifying the risk of hypoxic conditions for an irregular configuration of the microvessels. This conclusion is also supported by the dimensional analysis of the governing equations. Since oxygen transport in the interstitial volume is reaction dominated, regions free of oxygen sources will easily experience low oxygen supply. The visualization of oxygen concentration maps of Figure 3 can be directly compared with the results of [33], see in particular Figure 3A, obtained using an equivalent model for oxygen transport. As a preliminary and qualitative validation of our results, we observe that the contour plots of the calculated oxygen concentration look remarkably similar in the two cases. As expected, the TPZ concentration is significantly influenced by the distribution of oxygen concentration. The distribution of TPZ in the considered tissue sample seems to be more uniform than in the case of oxygen. Again, dimensional analysis supports this conclusion, because it shows that diffusion and reaction equivalently contribute to TPZ transport.

In spite of the difference between the governing mechanisms at the basis of oxygen and TPZ transport, the simulated concentration maps of these species share common traits. This may be explained by two concurrent factors. On one hand, both solutes are affected by the distribution of capillaries. On the other hand, the metabolization of TPZ increases in hypoxic regions. This effect sustains TPZ concentration gradients similar to the ones of oxygen, by turning off TPZ absorption where oxygen concentration is elevated, and promoting TPZ metabolization where oxygen is low. Finally, the inspection of metabolized TPZ, namely $M^{tpz}(t,x)$, shows that the objective of reaching the hypoxic regions with a chemotherapy agent is substantially achieved, see in Figure 3 (left). More precisely, oxygen and $M^{tpz}(t,x)$ maps show a complementary pattern. It means that most of TPZ is metabolized in hypoxic regions.

Before proceeding, we study the sensitivity of these results with respect to the boundary conditions applied on the artificial sections separating the interstitial volume from the exterior. The simulations reported in 3 (top row) are obtained using $-D_t\nabla c_t \cdot \mathbf{n} = \beta_c c_t$ with a positive value of β_c is provided in Table 2. We compare these results with Figure 3 (bottom row), showing the concentration maps when homogeneous Neumann conditions (no flux) are prescribed for the concentrations on the boundary of Ω. This is equivalent to set $\beta_c = 0$. A slight increase in the TPZ concentration field is observed, in agreement with the fact that the outgoing diffusive flux is set to zero with the choice $\beta_c = 0$. For a more quantitative comparison, we study the sensitivity of the total amount of metabolized TPZ, $\overline{M}^{tpz}(t)$. After injecting TPZ for 20 minutes, we calculate $\overline{M}^{tpz}(t) = 7.76838 \times 10^{-9}$ g/m^3 when using Robin boundary conditions and $\overline{M}^{tpz}(t) = 8.6685 \times 10^{-9}$ g/m^3 in the case of Neumann conditions. Owing to these results, we conclude that the parameter β_c is not a factor of primary importance to determine the concentrations of oxygen and TPZ and we will use Robin conditions for all the forthcoming simulations.

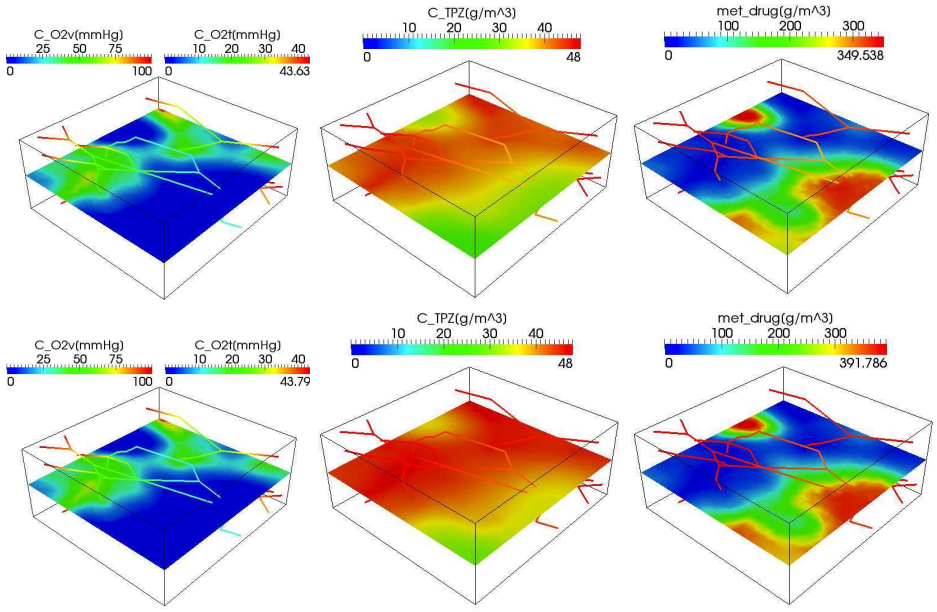

Figure 3: Oxygen concentration profile, TPZ concentration profile and metabolized drug profile are visualized from left to right. On the top row, simulations are performed using Robin boundary conditions for the concentrations of oxygen and TPZ at the boundary of the interstitial volume with the exterior. The results obtained using homogeneous Neumann conditions are depicted below.

3.3 Nanoparticle adhesion patterns and delivery of TPZ from nanoparticle injection

We split the analysis of the TPZ delivery from nanoparticles in two parts. First we focus on the nanoparticle adhesion model, with the aim to validate our results with respect to the ones reported in [22]. In a second phase, we analyze the concentration of TPZ delivered from the nanoparticles that decorate the capillary walls.

Nanoparticle adhesion is regulated by the vascular adhesion parameter Π, which in turn depends on the shear rate arising from the interaction of blood flow with the capillary walls. These two quantities are depicted in Figure 4. We observe that the wall shear rate features a significant spatial variation, although the capillary radius is constant along the network. This effect is due to the variable pressure, and consequently variable flow rate, along the network. We observe that the calculated values of wall shear rate fall in the physiological range [22]. According to the adopted adhesion model, the variability of wall shear rate is propagated to the adhesion parameter, reported on Figure 4 (left). As a result, we expect to observe a non uniform concentration of nanoparticles adhering to the wall.

The nanoparticle concentration, namely $\Psi(s,t)$, depends on the adhesion

parameter and on the particle concentration traveling through the vascular network. A preliminary validation of our simulations arises observing that the nanoparticle density per unit capillary surface, calculated for an injection phase lasting 20 seconds, is comparable to the one reported in [22]. To compare the delivery of TPZ from nanoparticles with the case of bolus injection, we consider a constant concentration of injected particles for 20 minutes. The analysis of adhered particles at 20 minutes after the initial time, shows that adhesion progressively increases. The results of Figure 4 (left and middle panels, bottom row) refer to the concentration of adhered nanoparticles normalized with respect to the injected value. On the right, we show the density of adhering particles when we consider the initial particle concentration C^{np}_{max}, which is calculated in order to match the the total flow of TPZ already used in the case of direct bolus injection.

Figure 5 shows the TPZ concentration delivered from nanoparticles at 20 seconds and 20 minutes after particle injection has started. Although the concentration levels are significantly different in the two cases, because of the time scales, the concentration maps share some similarities. In both cases, however, the geometry of the network can not be immediately related to the TPZ concentration map. Indeed, it is rather the distribution of the adhesion factor along the network, Π, that affects the calculated concentration field. Finally, the amount of metabolized TPZ shown in Figure 5 (right) seems to be rather independent from the previous factors, but mostly influenced by the oxygen concentration field.

3.4 Comparison of TPZ delivery from bolus and nanoparticle injection

The proposed model enables us to compare how the concentration of delivered drug varies in space and time for the two considered modalities of drug delivery. We also point out that, although the delivery pathway is different, the comparisons refer to the same amount of drug injected into the system.

In Figure 6 we visualize the TPZ concentration maps in the two cases, reported at 20 minutes, 40 minutes and at a final times comparable to the time at which there will be no longer drug to be delivered. The magnitude of the end time may differ in bolus and nanoparticle injection. The first time point corresponds to the instant when the injection of drug or particles into the vessels is turned off. The analysis of the results reveals some differences since the beginning of the delivery process. The drug concentration in the case of nanoparticle delivery is larger than the one of bolus delivery at all time points and the discrepancy increases with time.

Figure 6 also shows that the concentration of TPZ delivered from bolus injection rapidly vanishes after the injection is switched off. At 40 minutes after the injection has started, there is only a negligible trace of TPZ in the tissue, while after 6 hours the drug has completely vanished. This is clearly due to

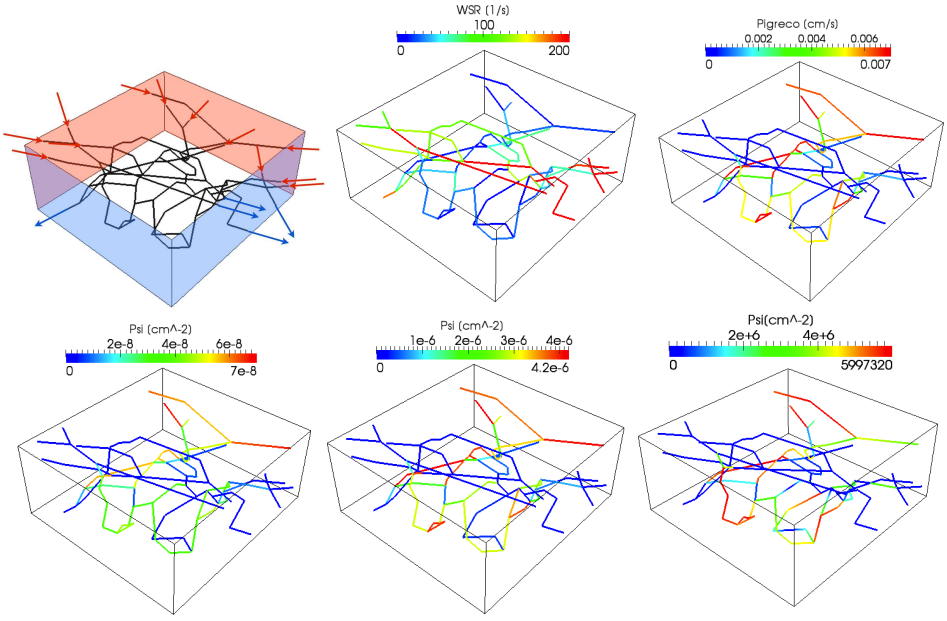

t=20 s
normalized C^{np}_{max}

t=20 min
normalized C^{np}_{max}

t=20 min
absolute C^{np}_{max}

Figure 4: Top panel: profiles of wall shear rate and vascular deposition parameter $\Pi(s)$ along the capillary network. Bottom, starting from the left: the density of nanoparticles decorating the wall, Ψ, at 20 seconds and at 20 minutes after nanoparticle injection has started. These values refer to a nominal unit concentration of injected particles ($\sharp/m^3$). Bottom right: Ψ at 20 minutes after injection for an inlet nanoparticle concentration equal to C^{np}_{max}.

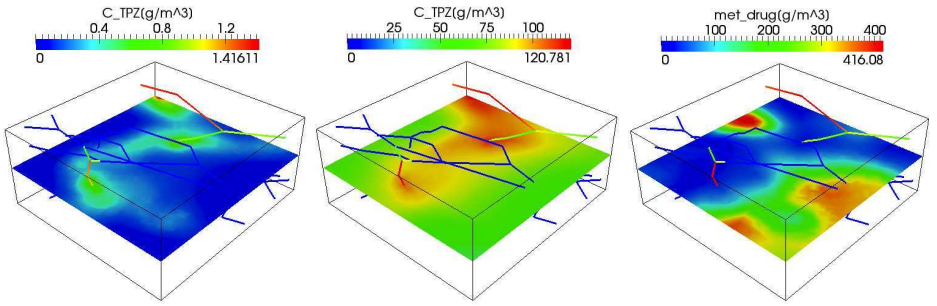

Figure 5: TPZ concentration maps at 20 seconds and 20 minutes after starting nanoparticle release (left and central panels). On the right we show the metabolized drug after 20 minutes. Robin boundary conditions are used in all cases.

drug metabolization. Surprisingly, TPZ drug concentration from bolus delivery is also lower at the first time point. The superior performance of the nanoparticle

delivery system on the short time scale can be justified by the role of nanoparticle adhesion. This effect helps to harvest drug from the blood stream and to store it on the capillary walls. As a result drug may be delivered in higher concentrations to the interstitial volume and at the same time a lower fraction of the injected drug is washed away by the blood stream leaving the tissue sample.

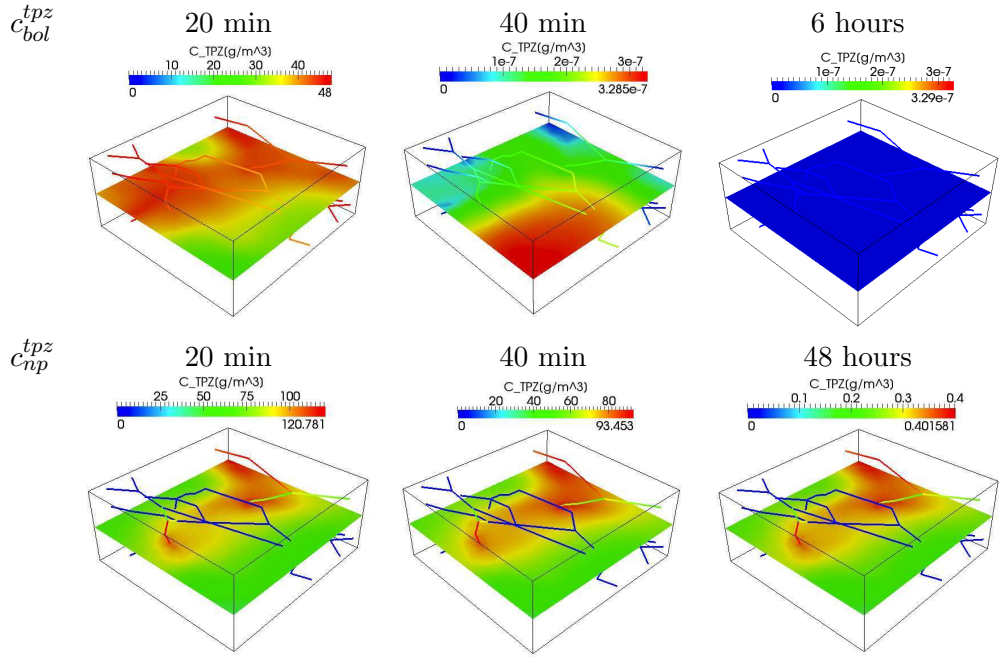

Figure 6: Comparison of TPZ concentrations released from bolus injection (subscript *bol*) and nanoparticle injection (subscript *np*).

In addition, the release rate from nanoparticles is more persistent. Drug will be delivered to the tissue over a period of time that is significantly longer than 20 minutes. This is due to the nanoparticle porous matrix, which represents a diffusional barrier to drug release. In this case, delivery and metabolization rates nearly balance, because the TPZ concentration in the interstitial volume slowly decreases for a period of almost 48 hours. This interpretation is supported by the visualization of the timecourse of the total drug amount available in the tissue, namely the volumetric integral of the TPZ concentration, reported in Figure 7. These results further highlight the inefficiency of drug bolus delivery when compared to drug delivery from nanoparticles.

The model suggests that bolus injection turns out to be a sub-optimal delivery strategy for two reasons. On one hand, tissue drug concentration rapidly reaches a plateau, much before the final injection time. The drug injected during this plateau phase is more likely to be washed out by the blood stream. On the other hand, the bolus injection system lacks of any buffer mechanism. Once the injection is switched off, drug levels rapidly decrease. In comparison, the

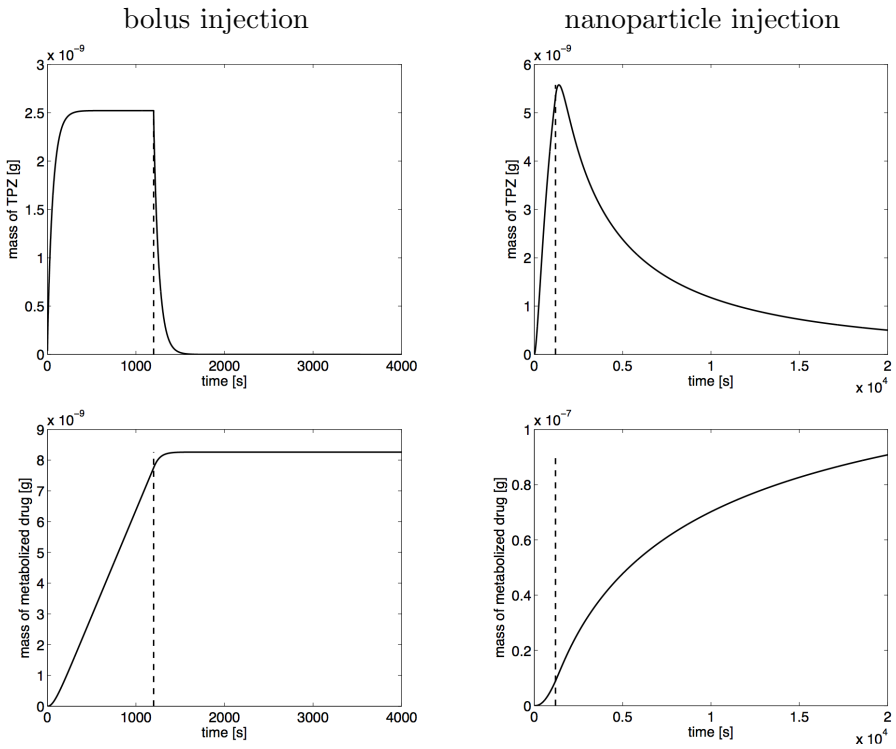

Figure 7: Comparison of systemic and nanoparticle release timecourses. The variation of $\int_\Omega c_t^{tpz}$ and $\overline{M}^{tpz}$ over time is visualized. The red line marks the time at which the injection of drug or particles into the vessels is stopped.

nanoparticle delivery system features two significant advantages. First, the particle adhesion mechanism allows for the accumulation of drug on the capillary walls. Secondly, the presence of particles decorating the capillary walls ensures a persistent drug release rate after that the injection of particles has stopped.

The profiles of TPZ concentration have a direct impact on the amount of metabolized drug. The maps of metabolized drug are shown in Figure 8. We observe that these maps look alike in all reported cases. This similarity confirms the dominant role of oxygen concentration to selectively activate the drug metabolization. However, the magnitude drastically changes from case to case. Since for the bolus delivery mode the drug supply to the tissue stops at 20 minutes, the amount of metabolized drug remains almost constant after this time. In contrast, the buffer effect provided by the adhered nanoparticles is responsible to a significant increase of metabolized drug over time. More precisely Figure 7 shows that $\overline{M}_{np}^{tpz}$ is about 10 times larger than $\overline{M}_{bol}^{tpz}$ 6 hours after injection. Similarly, from Figure 8 we observe that the pointwise values of M_{np}^{tpz} and M_{bol}^{tpz} scale by a factor 20 at 48 hours after delivery.

Finally, we compare the cell surviving fractions (SF) relative to bolus and nanoparticle injection. The cell surviving fraction depends on space and time,

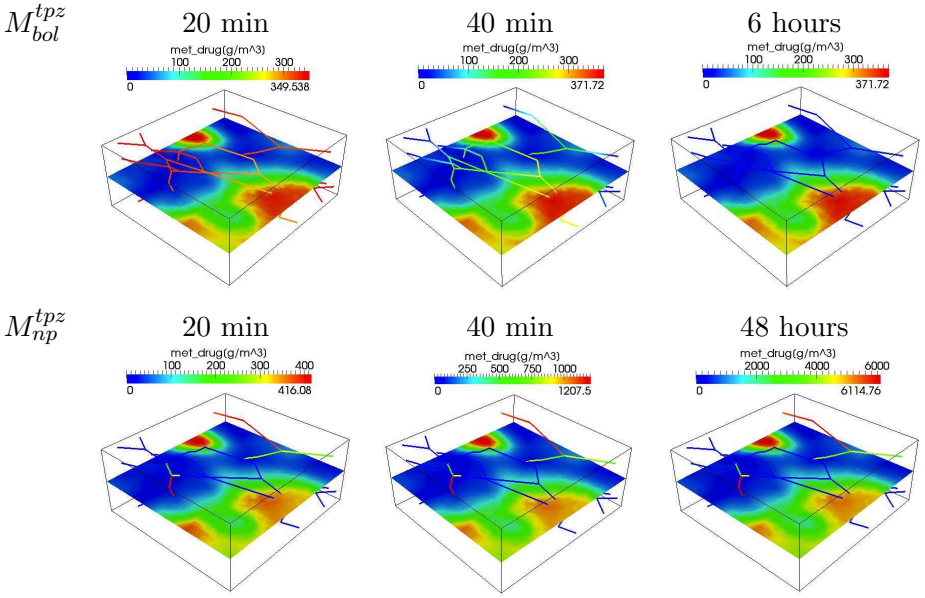

Figure 8: Comparison of metabolized TPZ released from bolus injection (subscript *bol*) and nanoparticle injection (subscript *np*).

but also on the oxygen availability. To selectively attack tumor mass, TPZ it targeted to treat hypoxic tissue. As shown in [21], it is convenient to plot the dependence of SF on oxygen partial pressure. This visualization of SF is displayed in Figure 9. The points of the diagram correspond to the nodes of the computational grid in the interstitial volume, denoted with $\boldsymbol{x}_i$. For each node, we extract the value of oxygen concentration and surviving fraction, at the final time,

$$(t = T, \boldsymbol{x}_i) \rightarrow c_t^{ox}(t = T, \boldsymbol{x}_i), \;\; SF(t = T, \boldsymbol{x}_i).$$

Then, in the diagrams of Figure 9 the surviving fraction is plotted with respect to the corresponding oxygen concentration, while the spatial information is hidden. As expected, SF sharply decreases for low oxygen concentrations, confirming that TPZ is able to selectively target hypoxic regions. The nanoparticle delivery mode results to be more effective also with respect to this indicator. On a short time scale, equivalent to the injection time, the efficacy of the bolus injection treatment is not particularly satisfactory because more than 50% of the cells still survive in hypoxic regions. For nanoparticle injection, the plot of SF after 20 minutes has a similar pattern, but the minimum of SF reaches 10%, confirming that this delivery modality is more effective. While the situation is almost unchanged for longer time scales in the case of bolus delivery, the performance further improves for nanoparticles on the time scale of 48 hours. Indeed, the SF profile has shifted downwards and its minimum reaches zero for low oxygen concentrations, meaning that almost all the cells in the interstitial volume are

treated. A slight drawback of the treatment based on nanoparticles can be detected looking at the distribution of the points in the SF plot. The dispersion of the point cloud increases and the slope of the underlying curve decreases with respect to the corresponding plot for bolus injection. This suggests that action of TPZ becomes less selective to target cells exposed to low oxygen concentration.

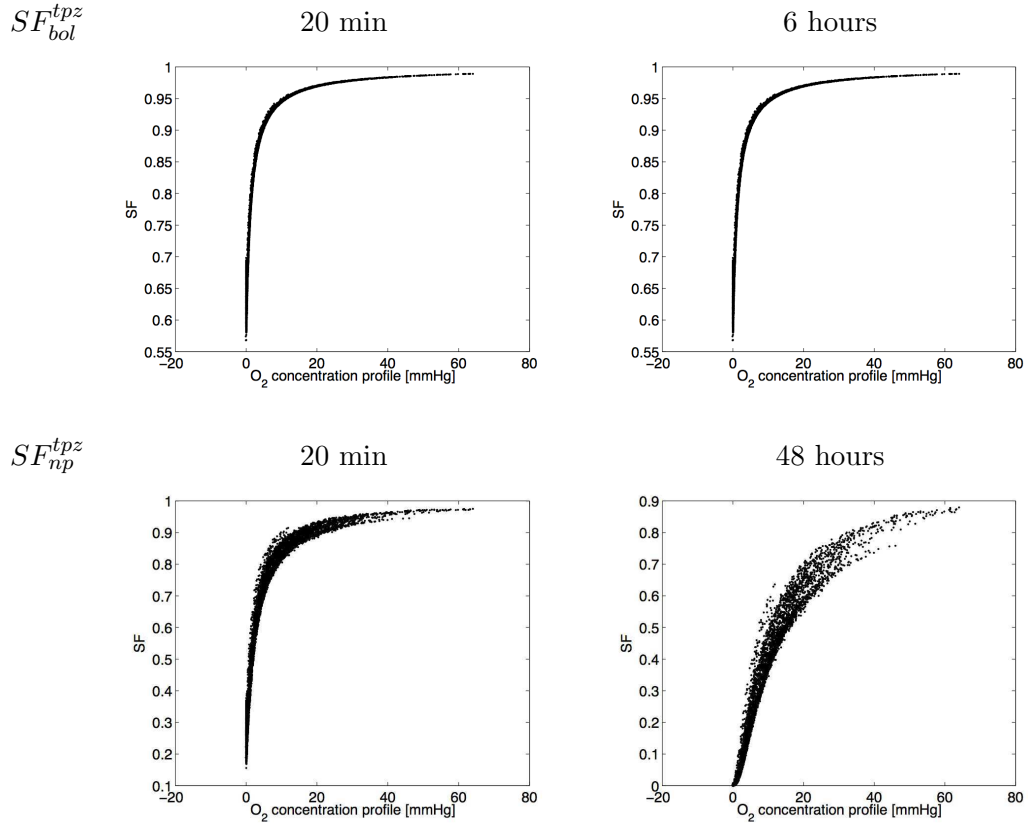

Figure 9: Comparison of cell surviving fraction (SF) when TPZ released from bolus injection (subscript *bol*) and nanoparticle injection (subscript *np*).

4 Conclusions, limitations and future perspectives

In this study we have developed a model capable to simulate the spatio-temporal evolution of drugs delivered to a tumor mass. The analysis is performed at the microscale, where the fundamental physics at the basis of flow and transport can be directly applied. We have used the model to compare bolus and nanoparticle injection for delivering chemotherapy agents. The model provides different insights on treatment performance, based on the analysis of specific quantitative indicators, such as the cell surviving fraction. On one hand, the model suggests that bolus injection does not ensure an optimal delivery. Drug washout

by the blood stream and saturation of the concentration level in the interstitial tissue play as limiting factors for the amount of drug that reaches the interstitial volume, where malignant cells are active. On the other hand, we observe that a more controlled drug delivery process, achieved by means of nanoparticle injection, helps to override the previous limitations.

Besides these encouraging results, the model is prone to several improvements. One line of development consists in coping with the rapid technological progress in designing innovative methods to efficiently and selectively deliver drugs [19, 37]. Indeed, the model can be extended to encompass different drug delivery platforms. Further ramifications of this study will also be devoted to develop specific models for different types of cancer. We expect that tumors developing in the brain, breast, liver or lungs may feature significant differences in their transport properties. The physiology of these organs as well as available metrics to characterize their transport properties will be combined to set up specific variants of the model for different tumors. Another limitation of the study consists to consider a tumor as a static environment. Future developments of the model will indeed consider the tumor microenvironment as a dynamic system where angiogenesis, cell proliferation and drug treatment constantly interact.

References

[1] M. Barzegar-Jalali, K. Adibkia, H. Valizadeh, M.R.S. Shadbad, A. Nokhodchi, Y. Omidi, G. Mohammadi, S.H. Nezhadi, and M. Hasan. Kinetic analysis of drug release from nanoparticles. *Journal of Pharmacy and Pharmaceutical Sciences*, 11(1):167–177, 2008.

[2] L.T. Baxter and R.K. Jain. Transport of fluid and macromolecules in tumors. i. role of interstitial pressure and convection. *Microvascular Research*, 37(1):77–104, 1989.

[3] L.T. Baxter and R.K. Jain. Transport of fluid and macromolecules in tumors ii. role of heterogeneous perfusion and lymphatics. *Microvascular Research*, 40(2):246–263, 1990.

[4] L.T. Baxter and R.K. Jain. Transport of fluid and macromolecules in tumors. iii. role of binding and metabolism. *Microvascular Research*, 41(1):5–23, 1991.

[5] L.T. Baxter and R.K. Jain. Transport of fluid and macromolecules in tumors: Iv. a microscopic model of the perivascular distribution. *Microvascular Research*, 41(2):252–272, 1991.

[6] T.R. Blake and J.F. Gross. Analysis of coupled intra- and extraluminal flows for single and multiple capillaries. *Mathematical Biosciences*, 59(2):173–206, 1982.

[7] P. Carmeliet and R.K. Jain. Angiogenesis in cancer and other diseases. *Nature*, 407(6801):249–257, 2000.

[8] L. Cattaneo and P. Zunino. Computational models for fluid exchange between microcirculation and tissue interstitium. *Networks and Heterogeneous Media*, 2013. to appear. Available as MOX Report 25/2013.

[9] D. Chapelle, J.-F. Gerbeau, J. Sainte-Marie, and I.E. Vignon-Clementel. A poroelastic model valid in large strains with applications to perfusion in cardiac modeling. *Computational Mechanics*, 46(1):91–101, 2010.

[10] S.J. Chapman, R.J. Shipley, and R. Jawad. Multiscale modeling of fluid transport in tumors. *Bulletin of Mathematical Biology*, 70(8):2334–2357, 2008.

[11] F.E. Curry. *Mechanics and thermodynamics of transcapillary exchange*, chapter 8, pages 309–374. Hand Book of Physiology. Am. Physiol. Soc., Bethesda., 1984.

[12] C. D'Angelo. *Multiscale modeling of metabolism and transport phenomena in living tissues*. Phd thesis, 2007.

[13] C. D'Angelo. Finite element approximation of elliptic problems with dirac measure terms in weighted spaces: Applications to one- and three-dimensional coupled problems. *SIAM Journal on Numerical Analysis*, 50(1):194–215, 2012.

[14] C. D'Angelo and A. Quarteroni. On the coupling of 1D and 3D diffusion-reaction equations. Application to tissue perfusion problems. *Math. Models Methods Appl. Sci.*, 18(8):1481–1504, 2008.

[15] G.J. Fleischman, T.W. Secomb, and J.F. Gross. The interaction of extravascular pressure fields and fluid exchange in capillary networks. *Mathematical Biosciences*, 82(2):141–151, 1986.

[16] G.J. Flieschman, T.W. Secomb, and J.F. Gross. Effect of extravascular pressure gradients on capillary fluid exchange. *Mathematical Biosciences*, 81(2):145–164, 1986.

[17] H.B. Frieboes, M. Wu, J. Lowengrub, P. Decuzzi, and V. Cristini. A computational model for predicting nanoparticle accumulation in tumor vasculature. *PLoS ONE*, 8(2), 2013.

[18] M.H. Friedman. *Principles and Models of Biological Transport*. Springer New York, 2008.

[19] S. Ganta, H. Devalapally, A. Shahiwala, and M. Amiji. A review of stimuli-responsive nanocarriers for drug and gene delivery. *Journal of Controlled Release*, 126(3):187–204, 2008.

[20] D. Hanahan and R.A. Weinberg. The hallmarks of cancer. *Cell*, 100(1):57–70, 2000.

[21] K.O. Hicks, F.B. Pruijn, T.W. Secomb, M.P. Hay, R. Hsu, J.M. Brown, W.A. Denny, M.W. Dewhirst, and W.R. Wilson. Use of three-dimensional tissue cultures to model extravascular transport and predict in vivo activity of hypoxia-targeted anticancer drugs. *Journal of the National Cancer Institute*, 98(16):1118–1128, 2006.

[22] S.S. Hossain, T.J.R. Hughes, and P. Decuzzi. Vascular deposition patterns for nanoparticles in an inflamed patient-specific arterial tree. *Biomechanics and Modeling in Mechanobiology*, pages 1–13, 2013.

[23] R.K. Jain, R.T. Tong, and L.L. Munn. Effect of vascular normalization by antiangiogenic therapy on interstitial hypertension, peritumor edema, and lymphatic metastasis: Insights from a mathematical model. *Cancer Research*, 67(6):2729–2735, 2007.

[24] Panos Macheras and Athanassios Iliadis. *Modeling in biopharmaceutics, pharmacokinetics, and pharmacodynamics*, volume 30 of *Interdisciplinary Applied Mathematics*. Springer, New York, 2006. Homogeneous and heterogeneous approaches.

[25] C. Michler, A.N. Cookson, R. Chabiniok, E. Hyde, J. Lee, M. Sinclair, T. Sochi, A. Goyal, G. Vigueras, D.A. Nordsletten, and N.P. Smith. A computationally efficient framework for the simulation of cardiac perfusion using a multi-compartment darcy porous-media flow model. *International Journal for Numerical Methods in Biomedical Engineering*, 29(2):217–232, 2013.

[26] J.A. Moore and C.R. Ethier. Oxygen mass transfer calculations in large arteries. *Journal of Biomechanical Engineering*, 119(4):469–475, 1997.

[27] L. Mu and S.S. Feng. A novel controlled release formulation for the anticancer drug paclitaxel (taxol): Plga nanoparticles containing vitamin e tpgs. *Journal of Controlled Release*, 86(1):33–48, 2003.

[28] Karl Perktold, Martin Prosi, and Paolo Zunino. Mathematical models of mass transfer in the vascular walls. In *Cardiovascular mathematics*, volume 1 of *MS&A. Model. Simul. Appl.*, pages 243–278. Springer Italia, Milan, 2009.

[29] Alfio Quarteroni, Riccardo Sacco, and Fausto Saleri. *Numerical mathematics*, volume 37 of *Texts in Applied Mathematics*. Springer-Verlag, New York, 2000.

[30] Y. Renard and J. Pommier. *Getfem++: a generic finite element library in c++, version 4.2 (2012).* http://download.gna.org/getfem/html/homepage/.

[31] T.W. Secomb. Microvascular network structures. www.physiology.arizona.edu/people/secomb/network.

[32] T.W. Secomb, R. Hsu, R.D. Braun, J.R. Ross, J.F. Gross, and M.W. Dewhirst. Theoretical simulation of oxygen transport to tumors by three-dimensional networks of microvessels. *Advances in Experimental Medicine and Biology*, 454:629–634, 1998.

[33] T.W. Secomb, R. Hsu, E.Y.H. Park, and M.W. Dewhirst. Green's function methods for analysis of oxygen delivery to tissue by microvascular networks. *Annals of Biomedical Engineering*, 32(11):1519–1529, 2004.

[34] R.J. Shipley and S.J. Chapman. Multiscale modelling of fluid and drug transport in vascular tumours. *Bulletin of Mathematical Biology*, 72(6):1464–1491, 2010.

[35] M. Soltani and P. Chen. Numerical modeling of interstitial fluid flow coupled with blood flow through a remodeled solid tumor microvascular network. *PLoS ONE*, 8(6), 2013.

[36] Q. Sun and G.X. Wu. Coupled finite difference and boundary element methods for fluid flow through a vessel with multibranches in tumours. *International Journal for Numerical Methods in Biomedical Engineering*, 29(3):309–331, 2013.

[37] V.P. Torchilin. Multifunctional nanocarriers. *Advanced Drug Delivery Reviews*, 64(SUPPL.):302–315, 2012.

[38] G. Vilanova, I. Colominas, and H. Gomez. Capillary networks in tumor angiogenesis: From discrete endothelial cells to phase-field averaged descriptions via isogeometric analysis. *International Journal for Numerical Methods in Biomedical Engineering*, 29(10):1015–1037, 2013.

MOX Technical Reports, last issues

Dipartimento di Matematica "F. Brioschi",
Politecnico di Milano, Via Bonardi 9 - 20133 Milano (Italy)

08/2014 Cattaneo, L; Zunino, P.
A computational model of drug delivery through microcirculation to compare different tumor treatments

07/2014 Agasisti, T.; Ieva, F.; Paganoni, A.M.
Heterogeneity, school-effects and achievement gaps across Italian regions: further evidence from statistical modeling

06/2014 Benzi, M.; Deparis, S.; Grandperrin, G.; Quarteroni, A.
Parameter estimates for the relaxed dimensional factorization preconditioner and application to hemodynamics

05/2014 Rozza, G.; Koshakji, A.; Quarteroni, A.
Free Form Deformation Techniques Applied to 3D Shape Optimization Problems

04/2014 Palamara, S.; Vergara, C.; Catanzariti, D.; Faggiano, E.; Centonze, M.; Pangrazzi, C.; Maines, M.; Quarteroni, A.
Patient-specific generation of the Purkinje network driven by clinical measurements: The case of pathological propagations

03/2014 Kashiwabara, T.; Colciago, C.M.; Dede, L.; Quarteroni, A.
Well-posedness, regulariy, and convergence analysis of the Finite Element approximation of a Generalized Robin boundary value problem

02/2014 Antonietti, P.F.; Sarti, M.; Verani, M.
Multigrid algorithms for high order discontinuous Galerkin methods

01/2014 Secchi, P.; Vantini, S.; Zanini, P.
Hierarchical Independent Component Analysis: a multi-resolution non-orthogonal data-driven basis

67/2013 Canuto, C.; Simoncini, V.; Verani, M.
On the decay of the inverse of matrices that are sum of Kronecker products

66/2013 Tricerri, P.; Dede ,L; Quarteroni, A.; Sequeira, A.
Numerical validation of isotropic and transversely isotropic constitutive models for healthy and unhealthy cerebral arterial tissues